

Co-delivery of fucoxanthin and Twist siRNA using hydroxyethyl starch-cholesterol self-assembled polymer nanoparticles for triple-negative breast cancer synergistic therapy

Zeliang Wu

Huazhong University of Science and Technology

Yuxiang Tang

Huazhong University of Science and Technology

Zhaozhao Chen

Huazhong University of Science and Technology

Yao Feng

Huazhong University of Science and Technology

Dianwen Yu

Huazhong University of Science and Technology

Hang Hu

Changzhou University

Hui Liu

Huazhong University of Science and Technology

Wei Chen

Huazhong University of Science and Technology

Yu Hu

Huazhong University of Science and Technology

Rong Xu

rongxu@hust.edu.cn

Huazhong University of Science and Technology

Research Article

Keywords: triple negative breast cancer, cancer-associated fibroblasts, fucoxanthin, Twist, small interfering RNA, hydroxyethyl starch, co-delivery strategy

Posted Date: November 9th, 2022

DOI: <https://doi.org/10.21203/rs.3.rs-2237290/v1>

License:  This work is licensed under a Creative Commons Attribution 4.0 International License.

[Read Full License](#)

Additional Declarations: No competing interests reported.

Version of Record: A version of this preprint was published at Journal of Advanced Research on April 1st, 2024. See the published version at <https://doi.org/10.1016/j.jare.2024.04.017>.

Abstract

Background: Triple-negative breast cancer (TNBC) represents the most aggressive subtype of breast cancer with an extremely dismal prognosis and few treatment options. As a desmoplastic tumor, tumor cells are girdled by stroma composed of tumor-associated fibroblasts (CAFs) and their secreted stromal components. The rapidly proliferating tumor cells, together with the tumor stroma, exert additional solid tissue pressure on tumor vasculature and surrounding tissues, severely obstructing therapeutic agent from deep intratumoral penetration, and resulting in tumor metastasis and treatment resistance. Fucoxanthin (FX), a xanthophyll carotenoid abundant in marine algae, has attracted widespread attention as a promising alternative candidate for tumor prevention and treatment. Twist is a pivotal regulator of epithelial to mesenchymal transition (EMT), and its depletion has proven to sensitize antitumor drugs, inhibit metastasis, reduce CAFs activation and the following interstitial deposition, increase tumor perfusion, and allow more drugs to be delivered across the tumor stroma.

Results: Herein, our studies proposed a novel self-assembled polymer nanoparticle (siTwist/FX@HES-CH NPs) based on the amino-modified hydroxyethyl starch (HES-NH₂) grafted with hydrophobic segment cholesterol (CH). Systematic studies demonstrated that the co-delivery strategy of natural product FX and nucleic acid drug Twist siRNA (siTwist) could not only synergistically kill tumor cells, but also inhibit the CAFs activation and extracellular matrix synthesis. Loose tumor stroma further facilitated transvascular transport and deep penetration of nanoparticles, obviously alleviating the primary tumor burden and inhibiting lung metastasis.

Conclusions: This dually functional nanomedicine that targets both tumor cells and tumor microenvironment (TME) could form a potent anti-TNBC therapeutic cyclical feedback loop, providing a new paradigm for TNBC treatment.

Introduction

According to the 2021 global cancer statistics report, breast cancer has surpassed lung cancer to become the most commonly diagnosed malignant carcinoma [1]. Triple-negative breast cancer (TNBC), the most aggressive subtype of breast cancer, is characterized by a deficiency in estrogen receptor (ER), progesterone receptor (PR), and human epidermal growth factor receptor 2 (HER2), and accounts for about 15-20% of all breast cancer cases [2, 3]. TNBC shows a poor prognosis due to its high molecular heterogeneity, metastatic potential, and relapse proneness, and the mortality rate within the first five years after diagnosis is around 40% [4, 5]. Furthermore, distant metastasis occurs in most of TNBC patients, which typically happens in the lungs, bones, and brain [5, 6]. Chemotherapy, the standard systemic treatment for TNBC, exhibits limited efficacy and high recurrence rates mainly due to the treatment resistance [6-8]. Moreover, owing to the lack of expression of all three receptors, TNBC was unable to effectively respond to endocrine therapy or trastuzumab treatment [9-11]. Therefore, the development of advanced strategies to improve the therapeutic effect of TNBC is highly desirable.

Natural compounds with tumor-suppressive capabilities are regarded to be a promising candidate to expand the TNBC therapeutic choices [12, 13]. Fucoxanthin (FX), a natural xanthophyll carotenoid that could be isolated broadly from marine brown algae and other macro-/microalgae, shows negligibly adverse effects in rodents or humans at therapeutic dosages [14-20]. FX's substantial anti-cancer potential is possibly due to the structure of the abundant allenic bond, which has been demonstrated in a variety of cancers, including breast cancer [21-29]. Mechanism studies confirmed that FX exerts a multi-target anti-tumor effect *via* classical pathways implicated in apoptosis induction, cell cycle arrest, anti-metastasis, and autophagy regulation [30, 31]. Our previous studies also proved that FX could improve chemotherapy sensitivity in non-small-cell lung cancer [32]. Besides, FX was able to act as an antilymphangiogenic agent to alleviate the tumor burden and lymphatic metastasis in the TNBC xenograft model [33]. Collectively, it is believed that FX with widespread sources and low side effects is expected to be used as a novel anti-cancer agent. Despite its promise, the unique allenic bond structure is relatively unstable and easily wrecked by heating, aerial exposure, or illumination [34-36]. Furthermore, sufficient accumulation and high penetration of agents into tumor tissue to achieve lethal effects is always challenged. The utilization of free FX revealed limited distribution, poor solubility and low bioavailability, all of which compromised its clinical application [29, 36-39]. Therefore, encapsulating FX in drug delivery systems could achieve substantial tumor accumulation while also improving FX efficacy.

Another important obstacle limiting the efficacy of conventional TNBC treatment regimens is the complicated tumor microenvironment (TME). Numerous evidence suggested that the TME is an "active participant" in tumor progression and antitumor drug resistance, rather than a "bystander" [40-42]. TNBC, as a desmoplastic tumor, is distinguished from others by the presence of a dense tumor stroma composed primarily of α -SMA⁺ cancer-associated fibroblasts (CAFs) and their derived stromal components [43]. By secreting chemokines, cytokines, and growth factors (*i.e.*, FGF, CXCL-10, IL-6, IL-8, and VEGF), CAFs remodel the tumor microenvironment, mediate interstitial deposition, induce abnormal tumor angiogenesis, trigger epithelial to mesenchymal transition (EMT), and finally promote tumor progression, metastasis, and drug resistance [44]. Moreover, CAFs synthesize abundant matrix proteins, which are then cross-linked into filaments and bundled into fibrils to generate a three-dimensional stroma network. Additionally, rapidly proliferating tumor cells, stromal cells, and dense interstitial deposits raise solid tissue pressure (STP), compressing perfusion vessels and limiting drug access to some tumors while allowing them to regenerate [45-47]. Therefore, remodeling the pathological TME may be an effective strategy for improving treatment outcomes in TNBC. Twist, a central regulator of EMT, is specificity overexpressed in TNBC and other tumor tissues [48-50]. Twist expression is a necessary and prerequisite condition for the transdifferentiation of normal quiescent fibroblasts to CAFs in breast cancers, as well as for the deposition of dense tumor stroma. Concurrently, activated CAFs also promoted Twist expression and activated EMT, invasion, and metastasis [51, 52]. Besides, Li *et al.* found that Twist depletion using RNA interference technology not only completely blocked the EMT but also partially reversed multidrug resistance in breast cancers [53]. Therefore, we hypothesized that depletion of Twist using small interfering RNA (siRNA) and combining it with FX treatment, all of which present dual effects on both tumor cells and TME, may serve as a promising strategy.

Nanotechnology-based drug delivery systems display superior advantages in improving the solubility and bioavailability of natural products, overcoming the *in vivo* delivery barrier of RNAi molecules, and enabling co-delivery of therapeutic agents owing to their encapsulation capability and simple modification strategies [54-56]. In this work, we constituted a FX and siTwist co-delivery nanovector by grafting biocompatible hydrophobic segment cholesterol (CH) onto hydroxyethyl starch (HES) (siTwist/FX@HES-CH) (**Scheme 1**). Intriguingly, we incorporated amino groups on HES composed of sugar units to expand the loading capability of negatively charged siRNA while also endowing HES-CH NPs with pH-sensitive properties (diameter variation), triggering an acidic tumor environment-responsive release. The systematic *in vitro* and *in vivo* therapeutic test confirmed that 100-200 nm siTwist/FX@HES-CH NPs could effortlessly accumulate in tumor tissue through enhanced permeability and retention (EPR) effects. Following the phenomenon, the co-delivered FX and siTwist not only eradicated TNBC cells synergistically but also effectively acted on fibroblasts, inhibiting their transdifferentiation into CAFs and remodeling the TME. This nanodrug delivery strategy forms a virtuous cyclic feedback loop in the treatment of TNBC. Tumor cell removal, CAFs inhibition, and ECM suppression result in brilliant STP reduction in the TME. Tumor blood vessel decompression allows more nanoparticles to be transported across the blood vessels, readily across the tumor stroma, and bind to tumor intracellular targets. Tumor cell destruction remodels the TME for deep drug penetration, resulting in remarkable anti-TNBC efficacy in primary tumor growth and the following lung metastasis.

Results And Discussion

2.1 Preparation and characterization of siRNA/FX@HES-CH NPs

Because of HES's hydrophilicity, biocompatibility, and PEG-like long-circulation properties, it is commonly used to fabricate drug carriers that improve the solubility and bioavailability of hydrophobic drugs *in vivo* [58, 59]. **Scheme S1** characterized the chemical synthesis of HES-CH nanovectors. The incorporation of amino groups on HES composed of sugar units has proven to improve the loading of negative drugs such as siRNA (amino groups were detected by ¹H-NMR characteristic). As shown in **Fig. 1A**, the successful synthesis of HES-NH₂ was validated by ¹H-NMR, the characteristic response signals of methylene in propylamine at 1.8 (a), 3.0 (b) appear in ¹H-NMR spectra of HES-NH₂, indicating the successful grafting of propylamine onto HES. The molar substitution (MS) of amine group was calculated by ¹H-NMR spectrum of HES-NH₂ in D₂O:

$$MS (NH_2) = \frac{\left(\frac{I_{\text{methylene}}}{2}\right)}{\left(\frac{I_{C_1H}}{1}\right)} \times 100\% \quad (1)$$

Where $I_{\text{methylene}}$ is the integral for the protons of the methylene group of propylamine (a) and I_{C_1H} is the integral for the protons linked to the C₁ carbon atom of HES (c). The MS of NH₂ is 20 % as determined

by $^1\text{H-NMR}$. CH-COOH was synthesized by grafting succinic acid onto cholesterol, molecular weight 509.36 was detected through high resolution mass spectrometer (HRMS) (**Fig. S1**), new signals of methylene in succinic acid between 2.4 and 2.5 appear in $^1\text{H-NMR}$ spectra (**Fig. 1B**), both indicating the successful synthesis of cholesterol-succinate.

The achievement of HES-CH was confirmed by $^1\text{H-NMR}$ and FT-IR. As shown in **Fig. 1C**, the protons of cholesterol between 0 and 2.5 appear in the $^1\text{H-NMR}$ spectrum of HES-CH. The FT-IR spectra (**Fig. 1D**) of HES-CH show the characteristic band of C=O stretching vibration of ester bond at 1731 cm^{-1} , C=O stretching vibration of amide bond and C=C stretching vibration at $1600\text{-}1700\text{ cm}^{-1}$ and N-H bending vibration of amide bond at 1533 cm^{-1} , indicating the successful conjugating of cholesterol onto HES.

The MS of CH was calculated by $^1\text{H-NMR}$ spectrum of HES-CH:

$$\text{MS (CH)} = \frac{\left(\frac{I_{\text{CH}}}{47}\right)}{\left(\frac{I_{\text{AGU}}}{3.8}\right)} \times 100\% \quad (2)$$

$$I_{\text{AGU}} = I - I_{\text{CH}} \times 2/47 \quad (3)$$

Where I_{CH} is the integral for the protons of CH between 0 and 2.5 ppm, and I_{AUC} is the integral for the protons linked to the C_1 carbon atom and hydroxyl protons of HES (c-f). I is the integral for the protons linked to the C_1 carbon atom of HES (f), hydroxyl protons of HES (c-e), the proton linked to the oxygen atom and the unsaturated proton of CH (a, b) between 4.5 and 6.0 ppm. The MS of CH of HES-CH is 14% as determined by $^1\text{H-NMR}$.

The titration result confirmed that the pKa of aminated HES-CH is around 8.1, and below this pH, aminated HES-CH was mainly positively charged. siRNA is negatively charged at pH 7.4, and thus can interact with aminated HES-CH electrostatically (**Fig. S2, A and B**). HES-CH NPs showed a +10 mV zeta potential at pH 7.2, +13 mV at pH 6.8, and +20 mV at pH 5.4, respectively (**Fig. S3A**). Amusingly, as the pH goes down from 7.2 to 5.4, the diameter of HES-CH NPs slightly increases from 100 nm to 120 nm (**Fig. S3B**). It is primarily attributed to the protonation of amino group, thus loosening the structure of HES-CH NPs. This property contributes to the accelerated releasing of agents at the acidic environment.

Table 1. Characterization of HES-CH, FX@HES-CH and siRNA/FX@HES-CH.

Formulations	Particle diameter (nm)	PDI	Zeta potential (mV)	EE (%)	DL (%)
HES-CH	118 ± 1.2	0.042	+11.3 ± 1.1	N/A	N/A
FX@HES-CH	136 ± 0.8	0.026	+10.8 ± 1.7	92.6 ± 1.7	7.38 ± 0.06
siRNA/FX@HES-CH	187 ± 2.7	0.118	+0.7 ± 0.2	96.9 ± 1.1	96.69 ± 0.74

FX was loaded into HES-CH using emulsion solvent evaporation method. As shown in Table 1, FX@HES-CH NPs shows a larger particle size of 136 ± 0.8 nm compared to the blank HES-CH NPs 118 ± 1.2 nm, indicating successful FX assembly. Since FX is electrically neutral, the Zeta potentials of FX@HES-CH NPs (+10.8 ± 1.7 mV) and HES-CH NPs (+11.3 ± 1.1 mV) are relatively closed. Subsequently, siRNA was loaded onto the surface of the FX@HES-CH NPs through electrostatic interactions to prepare siRNA/FX@HES-CH NPs. Encapsulation of siRNA resulted in a low positive Zeta potential (+0.7 ± 0.2 mV) and larger sizes (187 ± 2.7 nm), which is believed to reduce the interaction of the nanoparticles with the stromal components of the TME and making it more accessible to tumor cells. The calculated drug loading (DL%) of FX in FX@HES-CH NPs was 6.72 ± 0.3%, and the drug entrapment efficiency (EE%) of FX@HES-CH NPs and siRNA/FX@HES-CH NPs was greater than 90%. As shown in the agarose gel electrophoresis, when the HES-CH:siRNA (w/w) ratio was 80:1, about 96% of siRNA would effectively adhere to the HES-CH nanocarriers (**Fig. S4A**). Moreover, compared with the almost complete degradation of free siRNA in serum (<6 h) [60], the 48 h serum stability test revealed that loading siRNA with nanocarriers would effectively inhibit its degradation by nucleases in the serum (**Fig. S4B**). Furthermore, the nanostructure of siRNA/FX@HES-CH was imaged using transmission electron microscopy (TEM). A significant outer corona was observed on the siRNA/FX@HES-CH NPs, indicating a highly efficient loading of siRNA *via* electrostatic interactions. Besides, HES-CH NPs, FX@HES-CH NPs, and siTwist/FX@HES-CH NPs TEM images all showed the appropriate morphologies and size distributions (**Fig. 1E**).

2.2 *In vitro* cellular uptake

Although RNAi therapy has been identified as a promising cancer therapeutic technique, however, *in vivo* siRNA administration has proven to be a significant hurdle, restricting its practical applicability [61, 62]. Because of their anionic property, siRNAs would not spontaneously diffuse across cell membranes. Moreover, siRNA is highly unstable in the systemic circulation, which is rapidly destroyed by nucleases, and could elicit undesirable immunological responses [63]. Furthermore, aiming to exert functions effectively, siRNA should penetrate the cell membrane, then escape from the endosome, and uncomplex to interact with the target [61]. The high efficiency of the payload motivates us to investigate the cellular uptake of Cy5-labeled siRNA. The empty HES-CH were chosen as the control group to exclude the possibility of vehicle fluorescence interference. CLSM was used to observe 4T1 cells that has been treated with PBS, free Cy5-siNC, HES-CH, and Cy5-siNC@HES-CH, respectively. As shown in **Fig. S5A**, compared with the PBS, free Cy5-siNC or HES-CH treated cells (negligible fluorescence), cells incubated

with Cy5-siNC@HES-CH for 6 h displayed a strong visible red signals, and after 12 h of incubation, the red fluorescence of intracellular Cy5-siNC was clearly separated from the green fluorescence (Lyso-tracker Green), indicating that Cy5-siNC@HES-CH could induce siRNA escape from the lysosomal, possibly owing to the "proton sponge effect".

Furthermore, flow cytometry analysis was employed to quantitatively detect the cellular uptake of HES-CH NPs (**Fig. S5B**). After Cy5-siNC@HES-CH treatment, the cellular uptake efficiency of siRNA was up to 99.6%, which was approximately 4.45 times higher than that of free Cy5-siNC (22.4%). The non-specific cellular internalization of free siRNA may be ascribed to its aqueous solubility and lower molecular weight, but CLMS did not show visible red fluorescence under the same observation conditions. Based on the results, it is concluded that effective encapsulation of siRNA by HES-CH vectors could remarkably improve cellular uptake efficiency.

2.3 In vitro cytotoxicity

2.3.1. MTT assays

To assess the cancer cell drug delivery and synergistic anti-tumor efficacy of siTwist/FX@HES-CH, the *in vitro* cytotoxicity of free FX and siTwist/FX@HES-CH to 4T1 cells were evaluated by MTT assay. As shown in **Fig. 2 (A and B)**, the IC₅₀ of free FX at 24, 48, 72 h was 34.43, 17.87, and 9.61 μM, respectively, whereas the IC₅₀ of siTwist/FX@HES-CH at corresponding time was 26.00, 11.25, and 6.68 μM. siTwist/FX@HES-CH exhibited significantly improved cytotoxicity against 4T1 cells, and both formulations displayed a typical time- and dose-dependent cytotoxicity.

In addition, we also evaluated the viability of 4T1 cells after treatment with different treatments. As shown in **Fig. 2C**, compared with control group (PBS), 20 μM free FX displayed obvious anti-tumor activity, and this cytotoxicity was enhanced by co-delivering FX and siTwist, which was associated with the synergistic anti-tumor effect of the dual components. Moreover, compared with FX + siTwist group, this cytotoxicity was further enhanced by delivering FX and siTwist *via* HES-CH NPs to enhance cellular accumulation. The cytotoxicity difference between siNC/FX@HES-CH and siTwist/FX@HES-CH revealed that targeting the Twist gene could improve FX sensitivity. Furthermore, there is no substantial cytotoxicity after HES-CH nanovector treatment, indicating high biocompatibility of the HES-CH.

2.3.2. Viable and dead cells observations

The proportion of live and dead cells in 4T1 cells was directly observed after staining with Calcein-AM and PI solution. The green signal from hydrolyzed Calcein-AM stained the live cells, while the red signal from PI stained the dead cells. Notably, free FX showed a limited red and definite green fluorescence, indicating that FX alone possesses cytotoxicity. Nonetheless, after the combinative treatment, the remaining green fluorescence was shut down and replaced by red fluorescence, demonstrating that the cytotoxicity of FX was greatly enhanced by the co-delivery of siTwist. In addition, as expected,

fluorescence images of 4T1 cells revealed that the siTwist/FX@HES-CH combination therapy resulted in considerably more cell deaths (**Fig. 2, D and E**).

2.3.3. Apoptosis analysis

Furthermore, the pro-apoptotic performance to TNBC cells with siTwist/FX@HES-CH was systemically measured. The Annexin V-FITC/PI double stain was applied to detect cellular apoptotic stages. As shown in **Fig. 2 (F and G)**, groups of free FX, FX@HES-CH, and siNC/FX@HES-CH resulted in 12.27%, 21.78%, and 16.53% of apoptotic cells (in early or late apoptotic stages). This value for PBS control, siTwist and HES-CH were 4.15%, 6.14% and 4.62%, respectively, suggesting low toxicities of materials and siTwist. However, FX + siTwist and siTwist/FX@HES-CH presented higher apoptosis rates (29.00% and 44.90%, respectively.), which was attributed to the synergistic therapeutic effect of the siTwist and FX, as well as the enhanced internalization of dual components by the nano systems.

2.4 siTwist/FX@HES-CH inhibits TNBC cell migration and invasion

The migration and invasion ability of 4T1 cells *in vitro* was evaluated by the wound healing and the transwell assays. As shown in **Fig. 3 (A and B)**, the control group and HES-CH group healed the cell wound by about $67.06 \pm 5.97\%$ and $67.67 \pm 10.51\%$ after 36 h of incubation, respectively. FX and siTwist group, with healing rates of $54.23 \pm 2.89\%$ and $54.25 \pm 2.95\%$, respectively, intimating that free FX or siTwist delayed migration to the certain extent. FX and siRNA co-incubation ($31.30 \pm 2.18\%$ healing rate) obviously retarded the migration of 4T1 cells. More importantly, due to the successful encapsulation of HES-CH nanovectors, the healing rates of FX@HES-CH, siNC/FX@HES-CH and siTwist/FX@HES-CH were $40.47 \pm 5.74\%$, $43.69 \pm 6.57\%$, and $22.36 \pm 2.65\%$, respectively. Consistently, 4T1 cells showed a significant reduction in migration and invasion in the presence of siTwist/FX@HES-CH in both transwell migration and matrigel invasion assays (**Fig. 3, C, D, E and F**). The migration, invasion, and wound healing rates of the blank HES-CH group were comparable to those of the PBS-treated group, demonstrating that the vector materials showed little effect on cell movement. In general, tumor metastasis could be obviously inhibited by delivering FX and siTwist together *via* HES-CH nanovectors.

To verify that the synergistic inhibitory effect of siTwist/FX@HES-CH on TNBC cell migration and invasion was achieved by interfering with Twist protein, we evaluated the expression of Twist protein in 4T1 cells after treatment with siTwist/FX@HES-CH. As shown in **Fig. S6**, the FX + siTwist group inhibited Twist protein expression more effectively than free FX or siTwist. Furthermore, the siTwist/FX@HES-CH NPs treatment noticeably decreased the expression of Twist protein compared with other groups.

2.5 In vitro penetration and growth inhibition evaluation in three-dimensional multicellular tumor spheroids

4T1 cells & NIH/3T3 cells co-cultured hybrid tumor spheroids were established as the *in vitro* model to evaluate the solid tumor penetration of nanoparticles. To investigate the tumor parenchyma penetration ability of siTwist/FX@HES-CH nanoparticles, we synthesized Cy5-siNC/C6@HES-CH NPs with Cy5-siNC

(red) and coumarin 6 (C6, green) as fluorescent tracers instead of siTwist and FX, respectively. As shown in **Figs. (4 and S7)**, after 48 h incubation of Cy5-siNC/C6@HES-CH with PBS, siTwist@HES-CH (containing 100 nM siTwist) and siTwist/FX@HES-CH (containing 100 nM siTwist and 20 μ M FX) respectively, CLSM was employed to observe the deep penetration of nanoparticles into three-dimensional multicellular tumor spheroids. The results indicated that while Cy5-siNC/C6@HES-CH alone could penetrate the tumor spheroid, the depth of penetration was significantly increased by siTwist@HES-CH and was even more remarkable after siTwist/FX@HES-CH treatment.

The Twist's role in mediating TME remodeling has been well known. Considering the synergistic inhibition of Twist protein expression by siTwist/FX@HES-CH, we investigated whether this consequence would substantially modulate the TME. The TME of TNBC is primarily composed of α -SMA⁺ cancer-associated fibroblasts (CAFs) and stromal components derived from them [64]. Growth factors (PDG, TGF- β , *etc.*) secreted by tumor cells and immune infiltrating cells have been shown to induce fibroblasts to transdifferentiate into α -SMA⁺ CAFs [65-67]. To investigate the effect of siTwist/FX@HES-CH NPs on CAFs, the expression of α -SMA in different preparations-treated activated NIH/3T3 cells was detected [68]. As shown in **Fig. S8**, the expressions of α -SMA in activated NIH/3T3 cells decreased to a certain extent after FX and siTwist treatment, and the most significantly down-regulated occurred after administration of siTwist/FX@HES-CH NPs. In combination with the penetration research, it is speculated that the increased infiltration of tumor spheroids is induced by the reduction of solid tissue pressure and tumor microenvironment remodeling following siTwist and FX inhibition of tumor cell proliferation and CAF activation.

Cy5-siNC/C6@HES-CH. Tumor spheroids were incubated with Cy5-siNC/C6@HES-CH for 48 h, concurrently administered with PBS, siTwist@HES-CH (containing 100 nM siTwist) and siTwist/FX@HES-CH (containing 100 nM siTwist and 20 μ M FX). The tumor spheroid model was established by mixing 4T1 cells with NIH/3T3 fibroblasts. Green fluorescence represents C6, and red fluorescence represents Cy5-siNC.

In addition, we also evaluated the growth inhibition of three-dimensional multicellular tumor spheroids by different treatments. PBS, FX, HES-CH, siTwist@HES-CH, FX@HES-CH, and siTwist/FX@HES-CH were incubated with tumor spheroids for four days, respectively. As shown in **Fig. S9**, empty nanovectors and siTwist@HES-CH-treated spheroids performed similarly to the control group, with no significant growth inhibition. The free FX group inhibited the growth of tumor spheroids, but this effect was remarkably enhanced by FX@HES-CH and siTwist/FX@HES-CH. The siTwist/FX@HES-CH group and FX@HES-CH group even showed tumor spheroids depolymerization on day 3 and day 4, respectively.

2.6 *In vivo* biodistribution of nanoparticles

The drug accumulation in the pathological site is critical for the evaluation of targeting efficiency of nanomedicine. Aiming for qualitative observation, siTwist and FX were replaced in the HES-CH with 1,1'-dioctadecyl-3,3',3'-tetramethylindotricarbocyanine iodide (DiR). Free DiR presented intense fluorescence

in liver and spleen at 48 h, but the fluorescence signal was much weaker in the tumor. The DiR@HES-CH was also nonspecific distributed in the liver and spleen, but the intratumoral accumulation of DiR was obviously higher than other groups (**Fig. 5A**). Furthermore, the time-dependent biodistribution was also measured to predict accumulation and destination of HES-CH. DiR@HES-CH NPs was intravenously injected and the accumulated amount of DiR in tumor reached the maximum at 72 h after counting its relative average fluorescence intensity (**Fig. 5, B and C**). Isolated organ imaging revealed a consistent time-dependence profile (**Fig. 5, D and E**). The results indicated that HES-CH was able to target tumor *via* the size-dependent EPR effect and therapeutic agents in HES-CH could retain in tumor for > 96 h. The fluorescence was distributed in the core of tumor, implying that HES-CH would penetrate deeper into the tumor and be more effective for solid tumor therapy. Moreover, we discovered that a portion of the drug released by HES-CH was transported to the lung region, where fluorescence signals remained for 48 hours.

2.7 *In vivo* antitumor therapy of siTwist/FX@HES-CH

Previous studies demonstrated that siTwist/FX@HES-CH could efficiently accumulate in the tumor tissues, have high permeability, and are readily uptaken by tumor cells. Encouraged by these results, we examined the efficacy of siTwist/FX@HES-CH-mediated combination strategy *in vivo*. **Fig 6A** showed the schematic design of orthotopic tumor therapy model. The 4T1 model is the closest preclinical animal model to human TNBC [69]. 4T1 cells were injected into mouse mammary pads and established 4T1 tumor-bearing mice model one weeks later. The mice were randomly divided into six groups (n = 6), and each group was treated by injecting formulations into the tail vein once every three days for six times. As shown in **Fig. 6 (B, C and D)**, The control group (saline) showed continued tumor growth, confirming the successful model establishment. The tumor growth in the empty HES-CH group was comparable to the control group, indicating that the HES-CH had no therapeutic effect. Silencing of Twist gene expression by siTwist@HES-CH exhibited negligible effects on tumor growth. Besides, free FX also presented limited tumor suppression in the later stages of treatment. This may be attributed to its poor solubility and non-specific biodistribution. FX@HES-CH showed better anti-tumor effect compared with free FX due to the increased FX accumulation inside tumor cells. Moreover, siTwist/FX@HES-CH outperforms FX@HES-CH in tumor suppression because twist depletion might well overcome therapeutic resistance to antitumor drugs. In addition, compared to the weight loss of mice after repeated administration of FX (dissolved in DMSO), the siTwist/FX@HES-CH group had no obviously weight loss despite incorporating two therapeutic modalities into the HES-CH vectors (**Fig. 6E**). These results confirmed that the advantage of combinative therapy in controlling the growth of the primary tumor.

To further investigate the potential anti-tumor mechanisms of siTwist/FX@HES-CH, tumor tissues were analyzed by H&E and immunohistochemistry staining. As shown in **Fig. 6F**, extensive nuclear pyknosis and cancer necrosis occurred in the siTwist/FX@HES-CH-treated group, demonstrating the synergistic anti-tumor effect of siTwist/FX@HES-CH. Compared to the other groups, siTwist/FX@HES-CH treatment resulted in the highest TUNEL and lowest Ki67 expression in tumor tissues, indicating an increase in apoptotic cell death and a significant decrease in tumor proliferation. Furthermore, FX exhibits the ability

to suppress the differentiation of endothelial progenitor cells into endothelial cells, which involves the formation of new blood vessels [70, 71]. Meanwhile, Twist overexpression in breast cancer cells could also induce abnormal angiogenesis [72, 73]. Therefore, CD31 staining assays were performed to assess angiogenesis in tumors. Results indicating that single-agent treatment with free FX, siTwist@HES-CH or FX@HES-CH inhibited abnormal angiogenesis, which was enhanced by siTwist/FX@HES-CH combinative treatments. Subsequently, we investigated protein expression of Twist in the orthotopic tumor tissue. Both western blot and immunofluorescence revealed the the lowest expression in siTwist/FX@HES-CH treatment (**Figs. 7A, 8E and S10A**). These results indicated that siTwist/FX@HES-CH nanoparticles could significantly inhibit the growth of primary tumors by synergistically inhibiting tumor cell proliferation, promoting apoptosis and anti-angiogenesis.

In vivo distribution revealed that HES-CH nanoparticles circulated for a relatively long time and accumulated at tumor sites. However, in the case of fibrous tumors, such as breast and colon cancer, deep penetration into the tumor parenchyma was blocked by the dense tumor stroma. Inhibiting the activation of α -SMA⁺ CAFs could reduce the secretion of CAFs-derived stroma [74, 75]. Mitigating solid stress in the tumor mass decompresses the tumor blood vessels further, allowing for more intratumoral drug delivery and penetration [76]. Therefore, we investigated the expression levels of collagen and α -SMA in the tumor microenvironment of each group. α -SMA is a marker of CAF activation, which could promote the collagen deposition and cross-linking [77]. According to representative immunofluorescence images, siTwist/FX@HES-CH remarkably reduced the expression of α -SMA in tumor tissues (**Figs. 7C and S10B**). The collagen content in the siTwist/FX@HES-CH group was consistently lower than that in the Control, FX, HES-CH, siTwist@HES-CH, and FX@HES-CH groups (**Fig. 7B**). To summarize, siTwist/FX@HES-CH not only fight against the tumor synergistically, but it also inhibits CAF activation and collagen expression in the tumor microenvironment. Therefore, siTwist/FX@HES-CH presented a greater inhibitory effect on tumor growth than FX@HES-CH. Additionally, other major organs were also analyzed by H&E staining, and no obvious pathological damage was detected (**Fig. 11S**).

2.8 In vivo anti-metastasis evaluation of siTwist/FX@HES-CH NPs

In vitro experiments confirmed that co-delivery of FX and siTwist using HES-CH vectors significant inhibition tumor cells invasion and migration. Therefore, the anti-metastasis effect was assessed in the highly metastatic orthotopic 4T1 breast tumor model using a treatment schedule depicted in **Fig. 8A**. Mice were injected with different formulations *via* tail vein every 3 days and treated seven times respectively. The first day of treatment was defined as day 0. After 35 days of treatments, based on the number of lung metastases nodules and H&E staining results, we found significantly reduced number of lung metastasis in the siTwist/FX@HES-CH treated mice (**Fig. 8, B, C and D**). In summary, it is concluded that the inhibition of Twist expression by siTwist/FX@HES-CH can significantly reduce the lung metastasis of orthotopic tumors. These results validated that the FX and siTwist co-delivery by the pH-responsive and tumor-penetrating HES-CH nanoparticles is a highly effective and safe approach for metastatic breast cancer therapy.

Conclusion

In conclusion, we reported an ingenious nanotherapeutic strategy that incorporates the co-delivery of the natural active antitumor product FX and the nucleic acid molecule siTwist. On one hand, HES-CH nanovectors can carry two completely different therapeutic agents and effective accumulation in tumor tissue due to the positive charge, long systemic circulation, and tumor tissue-responsive drug release of aminated-modified HES. Additionally, the co-delivery strategy acts on both tumor cells and TME, forming a powerful anti-tumor cyclic feedback loop. Tumor cell killing, CAF inhibition, and extracellular matrix synthesis blockade together result in the solid tissue pressure decrease in the tumor microenvironment. Tumor blood vessel decompression facilitates the transport of the nanomedicines across the blood vessels and stroma, and their uptake by tumor cells. Nanomedicines destroy the tumor cells after drug release and alter the tumor microenvironment to facilitate deep tumor penetration, primary tumor burden reduction and lung metastasis prevention. This combinative strategy targeting both tumor cells and tumor stroma provides a new avenue for the treatment of TNBC, and also holds great promise in other stroma-rich tumor therapy.

Materials And Methods

4.1. Materials

HES with an average molecular weight (Mw) of 130 kDa and hydroxyethyl molar substitution (MS) of 0.4 was purchased from Wuhan HUST life Sci & Tech Co., Ltd (Wuhan, China). Bromopro pylamine hydrobromide, succinic anhydride, cholesterol, N-ethyl-N'-(3-dimethylaminopropyl) carbodiimide hydrochloride (EDCI, 98%), and polycaprolactone were purchased from Aladdin Reagent Inc. (Shanghai, China). FX was purchased from MedChemExpress Co., Ltd. (Shanghai, China). Small interfering RNA duplexes against Twist (siTwist) [5'-GCU GAG CAA GAU UCA GAC CTT-3' (sense)], negative control RNA (siNC), and Cy5-labeled siNC nonspecific to any gene [5'-UUC UCC GAA CGU GUC ACG UTT-3' (sense)] were all ordered from GenePharm Co., Ltd. (Shanghai, China). INTERFERin[®] transfection reagent was obtained from Polyplus-transfection Co., (France). The Calcein-AM/PI live cell/dead cell double staining kit, and Annexin V-fluorescein isothiocyanate/propidium iodide apoptosis detection Kit were all obtained from Dojindo China Co., Ltd. (Shanghai, China). The MTT cell proliferation and cytotoxicity assay kit, Hoechst 33258 and Lyso-Tracker green were obtained from Beyotime Biotechnology Co., Ltd. (Shanghai, China). Transforming growth factor- β (TGF- β) was obtained from PeproTech, Inc. (Jiangsu, China). The anti-Twist antibodies were purchased from Abcam (Cambridge, UK). Anti- α -SMA antibodies were purchased from Abmart (Shanghai, China). Anti-GAPDH antibodies were purchased from Proteintech Group, Inc. (Wuhan, China). DiR iodide [1,1-dioctadecyl-3,3,3,3-tetramethylindotricarbocyanine iodide] were purchased from AAT Bioquest, Inc.(CA, USA). All other chemicals were of analytical grade and used as received.

4.2. Synthesis of aminopropyl HES (HES-NH₂)

HES was dissolved in 6.2 mol NaOH solution at 0.5 g/L, cooled for 40 min at 4 °C, and 960 mg 3-bromopropylamine hydrobromide was added for the reaction. The mixture was then reacted for 20 min at 4 °C. Adjust the pH to 7.0 by adding 37% HCl solution. The grafted polysaccharide was recovered by cooling precipitation in anhydrous ethanol (4 °C). The precipitate was then freeze-dried after being redissolved in distilled water for dialysis. The amino group content was determined using hydrogen nuclear magnetic resonance spectroscopy (¹H-NMR) characteristic spectra.

4.3. Synthesis of carboxylated CH (CH-COOH)

0.5 g of cholesterol and 0.5 g of succinic anhydride were added to 10.0 mL of pyridine solution to dissolve, and the reaction was stirred at 70 °C for 3 h before being rotary evaporated to dryness. The precipitation obtained is dissolved in ethanol and rotated again, and the white final product is the carboxylated modified cholesterol (CH-COOH), which is freeze-dried.

4.4. Synthesis of hydroxyethyl starch-cholesterol polymer (HES-CH)

1 g CH-COOH and 1 g HES-NH₂ were dissolved in 10 mL DMSO, then 0.5 g 1-hydroxybenzotriazole (HOBT) and 0.5 g 1-ethyl-(3-Dimethylaminopropyl) carbodiimide hydrochloride (EDC) were added, the mixture was heated and reacted overnight to obtain hydroxyethyl starch grafted cholesterol polymer (HES-CH), and unreacted was removed by dialysis impurities. The reactant solution was freeze-dried to obtain hydroxyethyl starch coupled cholesterol polymer (HES-CH) powder. Fourier transform infrared spectroscopy (FT-IR) and ¹H-NMR were used to characterize the structure of HES-CH powder.

4.5. Preparation of FX@HES-CH self-assembled NPs

Emulsion solvent evaporation was used to produce FX@HES-CH NPs. In a nutshell, 100 mg HES-CH was dissolved in 100 mL deionized water, and 10 mg FX was dissolved in 10 mL chloroform mixture. A cell crushing apparatus was used for ultrasound during emulsification. Subsequently, the chloroform solvent in the emulsion was removed using the rotary evaporation method to obtain the suspension of FX@HES-CH. The prepared FX@HES-CH NPs were lyophilized to obtain FX@HES-CH freeze-dried powder. FX concentration was measured by UV spectrophotometer at 449 nm [57]. The following formula was used to calculate the drug loading content and entrapment efficiency of FX:

$$DL (Wt\%) = \frac{Wt (FX)}{Wt (FX@HES - CH)} \times 100$$

$$EE (Wt\%) = \frac{Wt (FX)}{\text{Weight of the feeding } FX} \times 100$$

Where, $Wt (FX)$ is the amount of FX entrapped by the HES-CH NPs and Wt

$(FX@HES-CH)$ is the total weight of FX and HES-CH NPs.

4.6. Loading siRNA onto FX@HES-CH NPs

FX@HES-CH was mixed with 1 mg/mL siRNA in different weight ratios (2.5, 5, 10, 20, 40, 60, 80, 100, w/w). After magnetically stirring for 30 min at 4 °C, the binding of FX@HES-CH to siRNA was tested using agarose gel electrophoresis.

For the serum degradation stability assay, siRNA solution and siRNA/FX@HES-CH NPs solution were treated with FBS (50%, v/v) at 37 °C. The sample was collected at each time point for agarose gel electrophoresis analysis.

4.7. Cell culture

Mouse triple-negative breast cancer cell line (4T1) and mouse embryonic fibroblasts line (NIH/3T3) were purchased from the Chinese Academy of Sciences Cell Bank (Shanghai, China). 4T1 cells and NIH/3T3 cells were cultured in RPMI-1640 medium and DMEM medium, respectively, at 37 °C in a humidified atmosphere of 5% CO₂. Both media were supplemented with 10% (v/v) fetal bovine serum (FBS), 100 U/mL penicillin, and 100 µg/mL streptomycin.

4.8. Cellular uptake and intracellular trafficking of nanoparticles

To understand the cell internalization of nanoparticles or free siRNA, 4T1 cells treated with Cy5-siNC@HES-CH was imaged using confocal laser scanning microscopy (CLSM, Fluoview FV3000, Olympus, Japan). Cells were first seeded at a density of 6×10^4 cells per well in glass-bottom dishes and cultured for 24 h. Cells were then treated with Cy5-siNC@HES-CH (100 nM Cy5-siNC) for another 6 or 12 h. PBS, free Cy5-siNC and HES-CH (empty vectors) were used as control. After incubation with NPs, cells were washed, and then Hoechst 33258 (1 µg/mL) and Lyso-Tracker Green (100 nM) were added and fixed in ice-cold PBS containing 2% paraformaldehyde for 10 min. Red fluorescence (λ_{ex}/em , 650 nm/670 nm) of Cy5-siNC, blue fluorescence of Hoechst 33258 (λ_{ex}/em , 346 nm/460 nm) and green fluorescence of LysoTracker Green (λ_{ex}/em , 504 nm/511 nm) were observed using CLSM.

Quantitative analysis of NPs internalized by 4T1 cells was performed using flow cytometry. Cells were placed at a density of 6×10^4 cells per well in 6-well cell culture plates and incubated for 12 h with PBS, Cy5-siNC (100 nM), HES-CH, Cy5-siNC@HES-CH (100 nM Cy5-siNC). All cells were harvested and washed 3 times with PBS. Data were acquired by a BD FACSAria™ flow cytometer and analyzed by FlowJo_V10 software.

4.9. Cytotoxicity assay

The MTT assay kit was utilized to confirm the *in vitro* synergic cytotoxicity of siTwist/FX@HES-CH. Briefly, 3×10^3 4T1 cells were seeded in each well of a 96-well cell culture plate and cultured overnight. Cells were then treated with FX or siTwist/FX@HES-CH at different concentrations for 24, 48, and 72 h. After that, 100 μ L of fresh medium containing 10 μ L of MTT was added to the each well for 4 h in the dark. Following the incubation, 100 μ L of Formazan lysis solution was added to each well, and incubated at 37 °C for 3 h, until all the purple crystals were dissolved. And finally, the absorbance at 450 nm was measured with a microplate reader (Multiskan FC, Thermo Scientific, USA).

The cytotoxicity of different formulations was also evaluated using the MTT assay. Briefly, 3×10^3 4T1 cells were seeded in each well of a 96-well cell culture plate and cultured at 37 °C in a 5% CO₂ incubator overnight. The cell culture media was then replaced with fresh media containing different drugs, including PBS, free FX, siTwist, free FX + siTwist, HES-CH, FX@HES-CH, siNC/FX@HES-CH, and siTwist/FX@HES-CH (FX concentration of 20 μ M, siTwist concentration of 100 nM). After another 48 h of incubation, cell viability was determined using MTT assay as described above.

4.10. Flow-cytometry apoptosis assay

Cell apoptosis was detected using the Annexin V-/FITC apoptosis detection kit. 4T1 cells were seeded at a density of 1×10^5 cells per well in 6-well cell culture plates and cultured at 37 °C in a 5% CO₂ incubator overnight. The cell culture media was then replaced with fresh media containing different drugs, including PBS, free FX, siTwist, free FX + siTwist, HES-CH, FX@HES-CH, siNC/FX@HES-CH, and siTwist/FX@HES-CH (FX concentration of 20 μ M, siTwist concentration of 100 nM). After another 36 h of incubation, the cells were harvested, washed twice with cold PBS, resuspended in 400 μ L Annexin V binding buffer, and stained with Annexin V-FITC/PI for 20 min at 2-8°C in the dark. Fluorescence was quantified by flow cytometer (BD FACSAria™, USA). The results were analyzed using FlowJo_V10 software.

4.11. Viable and dead cells observations

In order to intuitively assess cellular viability after treating with the various formulations, the Calcein-acetoxymethyl (AM) / propidium iodide (PI) double staining kit was used according to the manufacturer's protocol. In brief, 4T1 cells were seeded at a density of 1×10^5 cells per well in 6-well cell culture plates and cultured at 37 °C in a 5% CO₂ incubator overnight. Cells were then incubated with different

formulations for 48 h, and washed with PBS. Following that, cells were incubated with calcein-AM and PI solutions for 15 min at 37 °C, then washed with PBS and imaged with fluorescence microscope.

4.12. Wound-healing assay

For the wound-healing assay, 4T1 cells were seeded at a density of 2×10^5 cells/mL to 6-well cell culture plates and cultured for 24 h. When cells grew to 80% confluence, the cell monolayer was scraped by sterile 10 μ L pipette tips, and washed three times with cold PBS. Cells were then incubated with PBS, free FX, siTwist, free FX + siTwist, HES-CH, FX@HES-CH, siNC/FX@HES-CH, and siTwist/FX@HES-CH for another 36 h. Cells were imaged under an inverted microscope.

4.13. Transwell migration and invasion assays

The *in vitro* anti-metastatic efficacy of siTwist/FX@HES-CH NPs was measured in 4T1 cells by cell migration and invasion assays in an insert Transwell device. In brief, for the migration assay, 2×10^5 4T1 cells in 100 μ L serum-free medium were added to the upper chamber, and 600 μ L of medium containing 10% FBS was added to the lower chamber. PBS, free FX, siTwist, free FX + siTwist, HES-CH, FX@HES-CH, siNC/FX@HES-CH, and siTwist/FX@HES-CH were added in both chambers. Cells were cultured at a 37 °C incubator and allowed migration through the insert membrane for 24 h. For the invasion assay, the upper chamber was coated with diluted Matrigel by serum-free medium (1:10, 100 μ L/well, BD Biocoat), then 100 μ L serum-free medium containing 2×10^5 4T1 cells was added in the upper chamber, and the lower chamber was filled with 600 μ L medium with 10% FBS. PBS, free FX, siTwist, free FX + siTwist, HES-CH, FX@HES-CH, siNC/FX@HES-CH, and siTwist/FX@HES-CH were also added in both chambers, and the cells were incubated for 36 h. Non-migrated cells (on the upper chamber) were removed by swabs. Cells that had migrated or invaded were fixed with methanol and stained with 0.1% crystal violet, and cells were photographed and counted under an inverted microscope.

4.14. Western blot assay

Twist protein expression in 4T1 cells was determined by western blot analysis. Briefly, 4T1 cells were seeded at a density of 1.5×10^5 cells per well in 6-well cell culture plates and cultured overnight. The cell culture media was then replaced with fresh media containing different drugs, including PBS, free FX, siTwist, free FX + siTwist, HES-CH, FX@HES-CH, siNC/FX@HES-CH, and siTwist/FX@HES-CH (FX concentration of 20 μ M, siTwist concentration of 100 nM). After another 48 h of incubation, total cellular proteins were harvested, and the expression levels of Twist were determined by western-blot assay.

NIH/3T3 cells were seeded at a density of 2×10^5 cells per well in 6-well cell culture plates and cultured overnight. The medium was then replaced with fresh DMEM medium containing TGF- β (10 ng/mL) and pre-incubated at 37 °C. Following that, the cells were treated with PBS, free FX, siTwist, free FX + siTwist, and siTwist/FX@HES-CH for 48 h (FX concentration of 20 μ M, siTwist concentration of 100 nM). Total cellular proteins were harvested, and the expression levels of α -SMA were determined by western-blot assay.

To analyze the expression of Twist in the TNBC tumors, tumor-bearing mice were randomly assigned to six groups and were given *i.v.* with saline, free FX (15 mg/kg), HES-CH, siTwist@HES-CH (equivalent to 1 mg/kg siTwist), FX@HES-CH (equivalent to 15 mg/kg FX) or siTwist/FX@HES-CH (equivalent to 15 mg/kg FX or 1 mg/kg siTwist) on days 0, 3, 6, excised tumor tissue on the ninth day, and the target proteins were harvested and determined by western-blot assay.

4.15. *In vitro* penetration and inhibition evaluation in three-dimensional multicellular tumor spheroids (MCTSs)

In order to evaluate the effect of inhibiting the activity of cancer associated fibroblasts (CAFs) on drug penetration, we simulated the solid tumor microenvironment to establish hybrid multicellular tumor spheroids (MCTSs) model co-cultured with tumor cells (4T1) and fibroblasts (NIH/3T3), and then evaluated permeation of siTwist/FX@HES-CH NPs *in vitro*. Briefly, 80 μ L of hot sterile agarose solution (1.5%, w/v) were pre-plated in a 96-well plate. After cooling to room temperature for solidification, 4T1 cells and NIH/3T3 cells were mixed in 96-well plates and cultured into hybrid MCTSs in a 2:1 ratio. After MCTSs grew to appropriate sizes, siTwist@HES-CH (containing 100 nM siTwist) and siTwist/FX@HES-CH (containing 100 nM siTwist and 20 μ M FX) nanoparticles were incubated with MCTSs, respectively. At the same time, Cy5-NC/C6@HES-CH was also added to each group. After 48 h incubation at 37°C, MCTSs were washed with cold PBS and fixed with 4% paraformaldehyde. Subsequently, spheroids were scanned by CLSM from the top to the middle of the MCTSs. Each 4T1 & NIH/3T3 MCTS has a scan layer of 15 μ m.

The construction scheme of MCTSs for tumor spheroids inhibition is the same as described above. After the spheroids reached to appropriate sizes, they were divided into six groups, and PBS, FX, HES-CH, siTwist@HES-CH, FX@HES-CH, siTwist/FX@HES-CH (FX concentration of 20 μ M, siTwist concentration of 100 nM) were added to the medium, respectively. An inverted light microscope was used to image and record the diameter changes in MCTSs on a daily basis.

4.16. *In vivo* biodistribution of NPs

Animal studies were carried out in accordance with protocols approved by Huazhong University of Science and Technology's Institutional Animal Care and Use Committees (IACUC). Breast tumors were orthotopically implanted by injecting 2×10^5 4T1 cells into the mammary fat pad of female BALB/c mice (GemPharmatech, JiangSu, China). When the tumor volumes reached approximately 200 mm³, mice were randomized into three treatment groups and injected through the tail vein with PBS, free DiR iodide [1,1-dioctadecyl-3,3,3,3-tetramethylindotricarbocyanine iodide] (DiR, 1 mg/kg DiR), and DiR@HES-CH (1 mg/kg DiR). The mice were then euthanized at 48 h after injection, and their hearts, livers, spleens, lungs, kidneys, and tumors were collected. All of the organs were washed with cold PBS and photographed using an *in vivo* imaging system (Pearl Trilogy, LI-COR, USA).

In addition, when the tumor volumes reached approximately 200 mm³, tumor-bearing mice were randomized into eight groups (n = 3 per group), and injected through the tail vein with DiR@HES-CH NPs at a DiR dose of 1 mg/kg. All mice were euthanized and imaged at 1, 6, 12, 24, 36, 48, 72, and 96 h after injection. The mice were then sacrificed at various time points following injection, and tumors, along with other major organs (heart, liver, spleen, lung, and kidney), were collected for *ex vivo* imaging. All the organs were washed with cold PBS and photographed using an *in vivo* imaging system (Pearl Trilogy, LICOR, USA).

4.17. Orthotopic mouse tumor model and treatment

An orthotopic mouse tumor model was established by injecting 1×10⁵ 4T1 cells into the mammary fat pad of female BALB/c mice on day -7. When tumors growing reached approximately 70-100 mm³ in volume, mice were randomly assigned to six groups (n = 6) and were given *i.v.* with saline, free FX (15 mg/kg), HES-CH, siTwist@HES-CH (equivalent to 1 mg/kg siTwist), FX@HES-CH (equivalent to 15 mg/kg FX) or siTwist/FX@HES-CH (equivalent to 15 mg/kg FX or 1 mg/kg siTwist) on days 0, 3, 6, 9, 12, and 15. Body weight and tumor size were monitored every 3 days for a total of 7 times. Tumor length and width were measured by calipers, and tumor volume was calculated according to the formula: volume (mm³) = length × width² / 2. The mice were euthanized eighteen days following treatment, and the locally developed tumors were removed, rinsed with cold PBS, and imaged. Subsequently, the completely peeled tumors were fixed in PBS containing 4% formaldehyde. Tumor tissues and major organs (heart, liver, spleen, lung, and kidney) slices were stained with H&E for routine histology assay. Immunohistochemistry revealed TUNEL assay, Ki67, and CD31. Immunofluorescence was used to detect Twist and α-SMA expression in primary tumors, as well as Masson staining for collagen analyses.

4.18. siTwist/FX@HES-CH NPs suppress lung metastasis of TNBC

The breast cancer spontaneous metastasis mouse model was established followed by the same procedures as the previous model. When tumors growing reached approximately 100 mm³ in volume, the 4T1 tumor-bearing mice were randomly assigned to six groups (n = 5) and were administered *i.v.* with saline, free FX (15 mg/kg), HES-CH, siTwist@HES-CH (equivalent to 1 mg/kg siTwist), FX@HES-CH (equivalent to 15 mg/kg FX) or siTwist/FX@HES-CH (equivalent to 15 mg/kg FX or 1 mg/kg siTwist) on day 0, 3, 6, 9, 12, 15 and 18. All the animals were euthanized on day 35 after treatment. The lungs were removed, washed with cold PBS, and photographed. The metastasis-suppressive effects of NPs were evaluated by counting the number of metastatic foci on the lung and H&E staining.

4.19. Statistical analysis

All the experiments were repeated at least in triplicate. Data were expressed as mean ± standard deviation (SD). Results were analyzed by two-tailed Student's t-test for two groups and one-way ANOVA for multiple groups. *p < 0.05, **p < 0.01, ***p < 0.001, and ****p < 0.0001 were considered to be statistically significant. The samples/animals were allocated to experimental groups and processed randomly.

Abbreviations

Coumarin 6 (C6), cancer-associated fibroblasts (CAFs), cholesterol (CH), carboxylated cholesterol (CH-COOH), confocal laser scanning microscopy (CLSM), 1,1-dioctadecyl-3,3,3,3-tetramethylindotricarbocyanine (DiR), drug loading capability (DL%), encapsulation efficiency (EE%), estrogen receptor (ER), epithelial to mesenchymal transition (EMT), Fucoxanthin (FX), hydroxyethyl starch (HES), human epidermal growth factor receptor 2 (HER2), high resolution mass spectrometry (HRMS), multicellular tumor spheroids (MCTSs), molar substitution (MS), nanoparticles (NPs), polydispersity index (PDI), progesterone receptor (PR), solid tissue pressure (STP), transforming growth factor- β (TGF- β), tumor microenvironment (TME), transmission electron microscope (TEM), triple-negative breast cancer (TNBC), Small interfering RNA (siRNA), ^1H nuclear magnetic resonance spectra ($^1\text{H-NMR}$).

Declarations

Supplementary Information

Additional file 1: Additional information includes schematic diagram of the synthesis of hydroxyethyl starch-cholesterol (HES-CH) monomers, characterization of CH-COOH by HRMS, the pKa measurement of HES-CH NPs, HES-CH NPs variation at different pH, loading content of siRNA in HES-CH NPs assessed by agarose gel retardation assay, stability of siRNA@HES-CH NPs in serum cytotoxicity of nanoparticles, in vitro cellular uptake of nanoparticles, quantification of maximum cross-section fluorescence intensity of three-dimensional multicellular tumor spheroids, in vitro western-blot analysis of α -SMA expression, in vitro three-dimensional multicellular tumor spheroids growth inhibition, the quantitative analysis of Twist and α -SMA fluorescence intensity, and biosafety assessment.

Acknowledgements

Not applicable.

Author contributions

XR conceived the project and edited the manuscript. CW and HY performed writing-review and editing. WZL designed and performed the experiments, and wrote the manuscript. TYX and CZZ participated in research design and assisted in the preparation and characterization of nanoparticles. FYA and YDW assisted in animal experiments. HH and LH provided technical support. All authors read and approved the final manuscript.

Funding

This work was supported by grants from the National Natural Science Foundation of China (Grant number, 81974450), and Natural Science Foundation of Hubei Province for Distinguished Young Scholars (Grant number, 2018CFA032).

Availability of data and materials

Not applicable.

Ethics approval and consent to participate

Experimental design and animal protocols were approved by the Institutional Animal Care and Use Committee (IACUC) at Huazhong University of Science and Technology

Consent for publication

All authors have reviewed and approved this manuscript.

Competing interests

The authors declare no conflict of interest.

Author details

¹Department of Pharmacology, School of Basic Medicine, Tongji Medical College, Huazhong University of Science and Technology, Wuhan 430030, China. ²Institute of Hematology, Union Hospital, Tongji Medical College, Huazhong University of Science and Technology, Wuhan 430022, China. ³The Key Laboratory for Drug Target Researches and Pharmacodynamic Evaluation of Hubei Province, Wuhan 430030, China. ⁴Department of Integrated Traditional Chinese and Western Medicine, Tongji Hospital, Tongji Medical College, Huazhong University of Science and Technology, Wuhan, 430030, Hubei, China. ⁵Hubei clinical medical center of cell therapy for neoplastic disease, Wuhan, 430022, China. ⁶Wuhan Sian Medical Technology Co., Ltd, Wuhan, 430022, China. ⁷School of Pharmacy, Changzhou University, Changzhou, 213164, China.

Reference

1. Sung H, Ferlay J, Siegel RL, Laversanne M, Soerjomataram I, Jemal A, et al. Global Cancer Statistics 2020: GLOBOCAN Estimates of Incidence and Mortality Worldwide for 36 Cancers in 185 Countries. *CA Cancer J Clin.* 2021;71(3):209-49.
2. Sporikova Z, Koudelakova V, Trojanec R, Hajduch M. Genetic Markers in Triple-Negative Breast Cancer. *Clin Breast Cancer.* 2018;18(5):e841-e50.
3. Liu Y, Ma XX, Zhu YJ, Lv X, Wang PP, Feng LZ. pH-responsive nanomedicine co-encapsulated with Erlotinib and chlorin e6 can enable effective treatment of triple negative breast cancer via reprogramming tumor vasculature. *Chem Eng J.* 2022;437.
4. Chang-Qing Y, Jie L, Shi-Qi Z, Kun Z, Zi-Qian G, Ran X, et al. Recent treatment progress of triple negative breast cancer. *Prog Biophys Mol Biol.* 2020;151:40-53.

5. Dent R, Trudeau M, Pritchard KI, Hanna WM, Kahn HK, Sawka CA, et al. Triple-negative breast cancer: clinical features and patterns of recurrence. *Clin Cancer Res.* 2007;13(15 Pt 1):4429-34.
6. Lin NU, Claus E, Sohl J, Razzak AR, Arnaout A, Winer EP. Sites of distant recurrence and clinical outcomes in patients with metastatic triple-negative breast cancer: high incidence of central nervous system metastases. *Cancer.* 2008;113(10):2638-45.
7. Gluz O, Liedtke C, Gottschalk N, Pusztai L, Nitz U, Harbeck N. Triple-negative breast cancer—current status and future directions. *Ann Oncol.* 2009;20(12):1913-27.
8. Zhang L, Fang C, Xu XQ, Li AL, Cai Q, Long XH. Androgen Receptor, EGFR, and BRCA1 as Biomarkers in Triple-Negative Breast Cancer: A Meta-Analysis. *Biomed Res Int.* 2015;2015.
9. Yin L, Duan JJ, Bian XW, Yu SC. Triple-negative breast cancer molecular subtyping and treatment progress. *Breast Cancer Res.* 2020;22(1):61.
10. Chaudhary LN, Wilkinson KH, Kong A. Triple-Negative Breast Cancer: Who Should Receive Neoadjuvant Chemotherapy? *Surgical oncology clinics of North America.* 2018;27(1):141-53.
11. Slamon D, Eiermann W, Robert N, Pienkowski T, Martin M, Press M, et al. Adjuvant trastuzumab in HER2-positive breast cancer. *N Engl J Med.* 2011;365(14):1273-83.
12. Nishino H, Satomi Y, Tokuda H, Masuda M. Cancer control by phytochemicals. *Curr Pharm Des.* 2007;13(33):3394-9.
13. Chen H, Yang J, Yang Y, Zhang J, Xu Y, Lu X. The Natural Products and Extracts: Anti-Triple-Negative Breast Cancer in Vitro. *Chem Biodivers.* 2021;18(7):e2001047.
14. Miyashita K. Function of Marine Carotenoids. *Forum Nutr.* 2009;61:136-46.
15. Beppu F, Niwano Y, Tsukui T, Hosokawa M, Miyashita K. Single and repeated oral dose toxicity study of fucoxanthin (FX), a marine carotenoid, in mice. *J Toxicol Sci.* 2009;34(5):501-10.
16. Iio K, Okada Y, Ishikura M. Single and 13-Week Oral Toxicity Study of Fucoxanthin Oil from Microalgae in Rats. *Food Hyg Safe Sci.* 2011;52(3):183-9.
17. Ren RD, Azuma Y, Ojima T, Hashimoto T, Mizuno M, Nishitani Y, et al. Modulation of platelet aggregation-related eicosanoid production by dietary F-fucoidan from brown alga *Laminaria japonica* in human subjects. *Brit J Nutr.* 2013;110(5):880-90.
18. Abidov M, Ramazanov Z, Seifulla R, Grachev S. The effects of Xanthigen (TM) in the weight management of obese premenopausal women with non-alcoholic fatty liver disease and normal liver fat. *Diabetes Obes Metab.* 2010;12(1):72-81.
19. Functional Ingredients from Algae for Foods and Nutraceuticals. In: Dominguez H, editor. *Functional Ingredients from Algae for Foods and Nutraceuticals*: Woodhead Publ Ltd, Abington Hall Abington, Cambridge Cb1 6ah, Cambs, UK; 2013.
20. Okada T, Mizuno Y, Sibayama S, Hosokawa M, Miyashita K. Antiobesity effects of *Undaria* lipid capsules prepared with scallop phospholipids. *J Food Sci.* 2011;76(1):H2-6.
21. Mei C, Zhou S, Zhu L, Ming J, Zeng F, Xu R. Antitumor Effects of *Laminaria* Extract Fucoxanthin on Lung Cancer. *Mar Drugs.* 2017;15(2).

22. Yu RX, Hu XM, Xu SQ, Jiang ZJ, Yang W. Effects of fucoxanthin on proliferation and apoptosis in human gastric adenocarcinoma MGC-803 cells via JAK/STAT signal pathway. *Eur J Pharmacol.* 2011;657(1-3):10-9.
23. Kotake-Nara E, Kushiro M, Zhang H, Sugawara T, Miyashita K, Nagao A. Carotenoids affect proliferation of human prostate cancer cells. *J Nutr.* 2001;131(12):3303-6.
24. Ayyad SE, Ezmirly ST, Basaif SA, Alarif WM, Badria AF, Badria FA. Antioxidant, cytotoxic, antitumor, and protective DNA damage metabolites from the red sea brown alga *Sargassum* sp. *Pharmacognosy Res.* 2011;3(3):160-5.
25. Shimoda H, Tanaka J, Shan SJ, Maoka T. Anti-pigmentary activity of fucoxanthin and its influence on skin mRNA expression of melanogenic molecules. *J Pharm Pharmacol.* 2010;62(9):1137-45.
26. Liu CL, Huang YS, Hosokawa M, Miyashita K, Hu ML. Inhibition of proliferation of a hepatoma cell line by fucoxanthin in relation to cell cycle arrest and enhanced gap junctional intercellular communication. *Chem Biol Interact.* 2009;182(2-3):165-72.
27. Satomi Y, Nishino H. Implication of mitogen-activated protein kinase in the induction of G1 cell cycle arrest and gadd45 expression by the carotenoid fucoxanthin in human cancer cells. *Bba-Gen Subjects.* 2009;1790(4):260-6.
28. Neumann U, Derwenskus F, Flister VF, Schmid-Staiger U, Hirth T, Bischoff SC. Fucoxanthin, A Carotenoid Derived from *Phaeodactylum tricornutum* Exerts Antiproliferative and Antioxidant Activities In Vitro. *Antioxidants-Basel.* 2019;8(6).
29. Xiao H, Zhao JR, Fang C, Cao Q, Xing MC, Li X, et al. Advances in Studies on the Pharmacological Activities of Fucoxanthin. *Mar Drugs.* 2020;18(12).
30. Kumar SR, Hosokawa M, Miyashita K. Fucoxanthin: A Marine Carotenoid Exerting Anti-Cancer Effects by Affecting Multiple Mechanisms. *Mar Drugs.* 2013;11(12):5130-47.
31. Meresse S, Fodil M, Fleury F, Chenais B. Fucoxanthin, a Marine-Derived Carotenoid from Brown Seaweeds and Microalgae: A Promising Bioactive Compound for Cancer Therapy. *Int J Mol Sci.* 2020;21(23).
32. Ming JX, Wang ZC, Huang Y, Ohishi H, Wu RJ, Shao Y, et al. Fucoxanthin extracted from *Laminaria Japonica* inhibits metastasis and enhances the sensitivity of lung cancer to Gefitinib. *Journal of Ethnopharmacology.* 2021;265.
33. Wang J, Ma YH, Yang JS, Jin L, Gao ZX, Xue LY, et al. Fucoxanthin inhibits tumour-related lymphangiogenesis and growth of breast cancer. *J Cell Mol Med.* 2019;23(3):2219-29.
34. Wang CY, Chen X, Nakamura Y, Yu CX, Qi H. Fucoxanthin activities motivate its nano/micro-encapsulation for food or nutraceutical application: a review. *Food Funct.* 2020;11(11):9338-58.
35. Li H, Xu Y, Sun X, Wang SH, Wang JW, Zhu JX, et al. Stability, bioactivity, and bioaccessibility of fucoxanthin in zein-caseinate composite nanoparticles fabricated at neutral pH by antisolvent precipitation. *Food Hydrocolloid.* 2018;84:379-88.
36. Koo SY, Mok IK, Pan CH, Kim SM. Preparation of Fucoxanthin-Loaded Nanoparticles Composed of Casein and Chitosan with Improved Fucoxanthin Bioavailability. *J Agr Food Chem.*

- 2016;64(49):9428-35.
37. Hashimoto T, Ozaki Y, Mizuno M, Yoshida M, Nishitani Y, Azuma T, et al. Pharmacokinetics of fucoxanthinol in human plasma after the oral administration of kombu extract. *Brit J Nutr.* 2012;107(11):1566-9.
 38. Hashimoto T, Ozaki Y, Taminato M, Das SK, Mizuno M, Yoshimura K, et al. The distribution and accumulation of fucoxanthin and its metabolites after oral administration in mice. *Brit J Nutr.* 2009;102(2):242-8.
 39. Salvia-Trujillo L, Sun Q, Urn BH, Park Y, McClements DJ. In vitro and in vivo study of fucoxanthin bioavailability from nanoemulsion-based delivery systems: Impact of lipid carrier type. *J Funct Foods.* 2015;17:293-304.
 40. Deepak KGK, Vempati R, Nagaraju GP, Dasari VR, Nagini S, Rao DN, et al. Tumor microenvironment: Challenges and opportunities in targeting metastasis of triple negative breast cancer. *Pharmacol Res.* 2020;153.
 41. Hui LL, Chen Y. Tumor microenvironment: Sanctuary of the devil. *Cancer Letters.* 2015;368(1):7-13.
 42. Minchinton AI, Tannock IF. Drug penetration in solid tumours. *Nat Rev Cancer.* 2006;6(8):583-92.
 43. Yu TJ, Di GH. Role of tumor microenvironment in triple-negative breast cancer and its prognostic significance. *Chinese J Cancer Res.* 2017;29(3):237-52.
 44. Mendes BB, Sousa DP, Coniot J, Conde J. Nanomedicine-based strategies to target and modulate the tumor microenvironment. *Trends Cancer.* 2021;7(9):847-62.
 45. Conklin MW, Eickhoff JC, Riching KM, Pehlke CA, Eliceiri KW, Provenzano PP, et al. Aligned Collagen Is a Prognostic Signature for Survival in Human Breast Carcinoma. *Am J Pathol.* 2011;178(3):1221-32.
 46. Stylianopoulos T, Jain RK. Combining two strategies to improve perfusion and drug delivery in solid tumors. *Proceedings of the National Academy of Sciences of the United States of America.* 2013;110(46):18632-7.
 47. Diop-Frimpong B, Chauhan VP, Krane S, Boucher Y, Jain RK. Losartan inhibits collagen I synthesis and improves the distribution and efficacy of nanotherapeutics in tumors. *Proceedings of the National Academy of Sciences of the United States of America.* 2011;108(7):2909-14.
 48. Glackin CA. Targeting the Twist and Wnt signaling pathways in metastatic breast cancer. *Maturitas.* 2014;79(1):48-51.
 49. Zhu QQ, Ma CH, Wang Q, Song Y, Lv TF. The role of TWIST1 in epithelial-mesenchymal transition and cancers. *Tumor Biol.* 2016;37(1):185-97.
 50. Pei HX, Li YQ, Liu MY, Chen YH. Targeting Twist expression with small molecules. *Medchemcomm.* 2017;8(2):268-75.
 51. Lee KW, Yeo SY, Sung CO, Kim SH. Twist1 Is a Key Regulator of Cancer-Associated Fibroblasts. *Cancer Res.* 2015;75(1):73-85.

52. Butti R, Nimma R, Kundu G, Bulbule A, Kumar TVS, Gunasekaran VP, et al. Tumor-derived osteopontin drives the resident fibroblast to myofibroblast differentiation through Twist1 to promote breast cancer progression. *Oncogene*. 2021;40(11):2002-17.
53. Li QQ, Xu JD, Wang WJ, Cao XX, Chen Q, Tang F, et al. Twist1-Mediated Adriamycin-Induced Epithelial-Mesenchymal Transition Relates to Multidrug Resistance and Invasive Potential in Breast Cancer Cells. *Clin Cancer Res*. 2009;15(8):2657-65.
54. Xin Y, Huang M, Guo WW, Huang Q, Zhang LZ, Jiang G. Nano-based delivery of RNAi in cancer therapy. *Mol Cancer*. 2017;16.
55. Yap KM, Sekar M, Fuloria S, Wu YS, Gan SH, Rani NNIM, et al. Drug Delivery of Natural Products Through Nanocarriers for Effective Breast Cancer Therapy: A Comprehensive Review of Literature. *Int J Nanomed*. 2021;16:7891-941.
56. Chen Y, Zhao TY, Bai MY, Gu TR, Sun J, He ZG, et al. Emerging small molecule-engineered hybrid nanomedicines for cancer therapy. *Chem Eng J*. 2022;435.
57. Sui Y, Gu Y, Lu Y, Yu C, Zheng J, Qi H. Fucoxanthin@Polyvinylpyrrolidone Nanoparticles Promoted Oxidative Stress-Induced Cell Death in Caco-2 Human Colon Cancer Cells. *Mar Drugs*. 2021;19(2).
58. Paleos CM, Sideratou Z, Tsiourvas D. Drug Delivery Systems Based on Hydroxyethyl Starch (vol 28, pg 1611, 2017). *Bioconjugate Chem*. 2017;28(8):2208-9.
59. Wang HM, Hu H, Yang H, Li ZF. Hydroxyethyl starch based smart nanomedicine. *Rsc Adv*. 2021;11(6):3226-40.
60. Wang YZ, Xie Y, Kilchrist KV, Li J, Duvall CL, Oupicky D. Endosomolytic and Tumor-Penetrating Mesoporous Silica Nanoparticles for siRNA/miRNA Combination Cancer Therapy. *Acs Appl Mater Inter*. 2020;12(4):4308-22.
61. Whitehead KA, Langer R, Anderson DG. Knocking down barriers: advances in siRNA delivery. *Nat Rev Drug Discov*. 2009;8(2):129-38.
62. Juliano R, Bauman J, Kang H, Ming X. Biological Barriers to Therapy with Antisense and siRNA Oligonucleotides. *Mol Pharmaceut*. 2009;6(3):686-95.
63. Watts JK, Deleavey GF, Damha MJ. Chemically modified siRNA: tools and applications. *Drug Discov Today*. 2008;13(19-20):842-55.
64. Yu T, Di G. Role of tumor microenvironment in triple-negative breast cancer and its prognostic significance. *Chin J Cancer Res*. 2017;29(3):237-52.
65. Shiga K, Hara M, Nagasaki T, Sato T, Takahashi H, Takeyama H. Cancer-Associated Fibroblasts: Their Characteristics and Their Roles in Tumor Growth. *Cancers*. 2015;7(4):2443-58.
66. Grinnell F, Billingham RE, Burgess L. Distribution of fibronectin during wound healing in vivo. *J Invest Dermatol*. 1981;76(3):181-9.
67. Kuzet SE, Gaggioli C. Fibroblast activation in cancer: when seed fertilizes soil. *Cell Tissue Res*. 2016;365(3):607-19.

68. Geng XL, Chen HZ, Zhao L, Hu JS, Yang WB, Li GQ, et al. Cancer-Associated Fibroblast (CAF) Heterogeneity and Targeting Therapy of CAFs in Pancreatic Cancer. *Front Cell Dev Biol.* 2021;9.
69. Pulaski BA, Ostrand-Rosenberg S. Mouse 4T1 breast tumor model. *Curr Protoc Immunol.* 2001;Chapter 20:Unit 20 2.
70. Jang H, Choi J, Park JK, Won G, Seol JW. Fucoxanthin Exerts Anti-Tumor Activity on Canine Mammary Tumor Cells via Tumor Cell Apoptosis Induction and Angiogenesis Inhibition. *Animals (Basel).* 2021;11(6).
71. Sugawara T, Matsubara K, Akagi R, Mori M, Hirata T. Antiangiogenic activity of brown algae fucoxanthin and its deacetylated product, fucoxanthinol. *J Agr Food Chem.* 2006;54(26):9805-10.
72. Mironchik Y, Winnard PT, Vesuna F, Kato Y, Wildes F, Pathak AP, et al. Twist overexpression induces in vivo angiogenesis and correlates with chromosomal instability in breast cancer. *Cancer Res.* 2005;65(23):10801-9.
73. Wang YF, Liu JY, Ying XH, Lin PC, Zhou BHP. Twist-mediated Epithelial-mesenchymal Transition Promotes Breast Tumor Cell Invasion via Inhibition of Hippo Pathway. *Sci Rep-Uk.* 2016;6.
74. Cai XJ, Wang Z, Xu YY, Yang GY, Zhang RY, Wang Y. Candesartan treatment enhances liposome penetration and anti-tumor effect via depletion of tumor stroma and normalization of tumor vessel. *Drug Deliv Transl Res.* 2021;11(3):1186-97.
75. Sharma M, Turaga RC, Yuan Y, Satyanarayana G, Mishra F, Bian Z, et al. Simultaneously targeting cancer-associated fibroblasts and angiogenic vessel as a treatment for TNBC. *J Exp Med.* 2021;218(4).
76. Zhu Y, Yu FY, Tan YN, Hong Y, Meng TT, Liu YP, et al. Reversing activity of cancer associated fibroblast for staged glycolipid micelles against internal breast tumor cells. *Theranostics.* 2019;9(23):6764-79.
77. Egeblad M, Rasch MG, Weaver VM. Dynamic interplay between the collagen scaffold and tumor evolution. *Curr Opin Cell Biol.* 2010;22(5):697-706.

Scheme 1

Scheme 1 is available in Supplementary Files section.

Figures

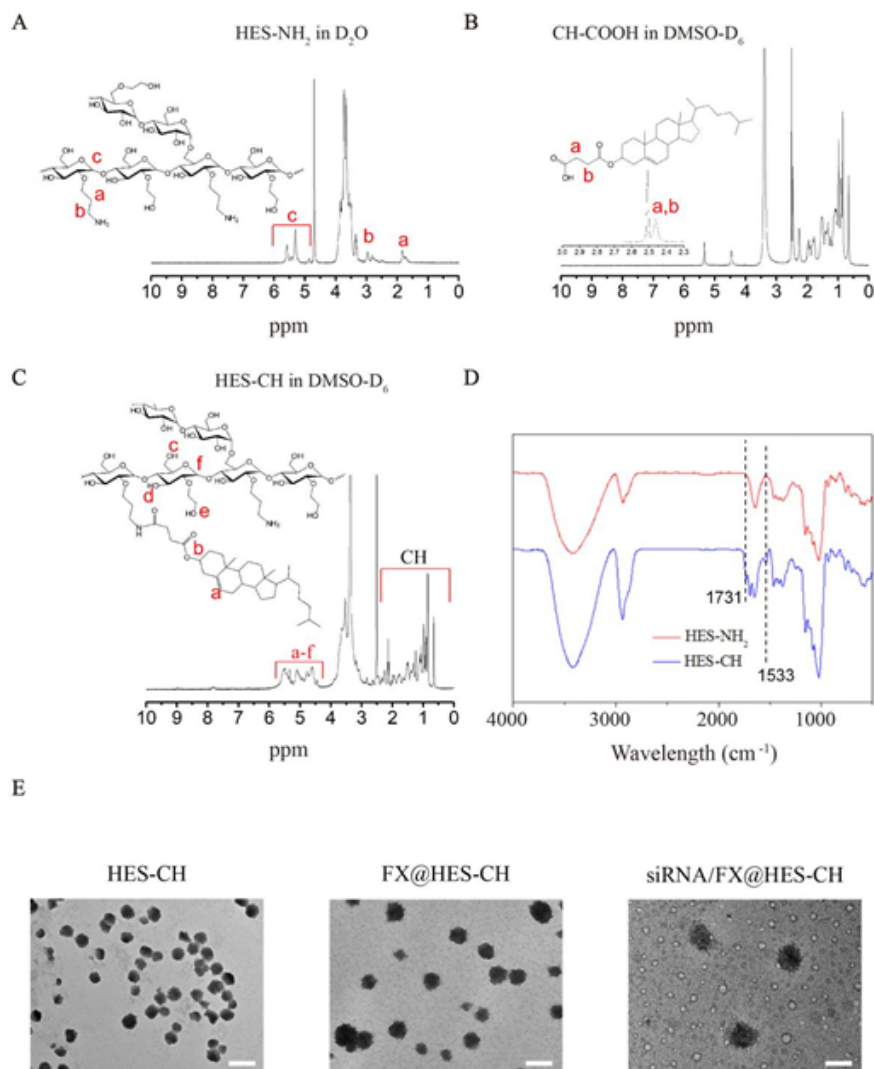


Figure 1

Synthesis of siRNA/FX@HES-CH. (A) $^1\text{H-NMR}$ spectra of HES- NH_2 in D_2O . (B) $^1\text{H-NMR}$ spectra of succinyl CH-COOH in DMSO-D_6 . (C) $^1\text{H-NMR}$ spectra of HES-CH in DMSO-D_6 . (D) FT-IR spectra of HES- NH_2 and HES-CH. (E) TEM images of HES-CH, FX@HES-CH, and siRNA/FX@HES-CH stained with phosphotungstic acid. Scale bar, 200 nm.

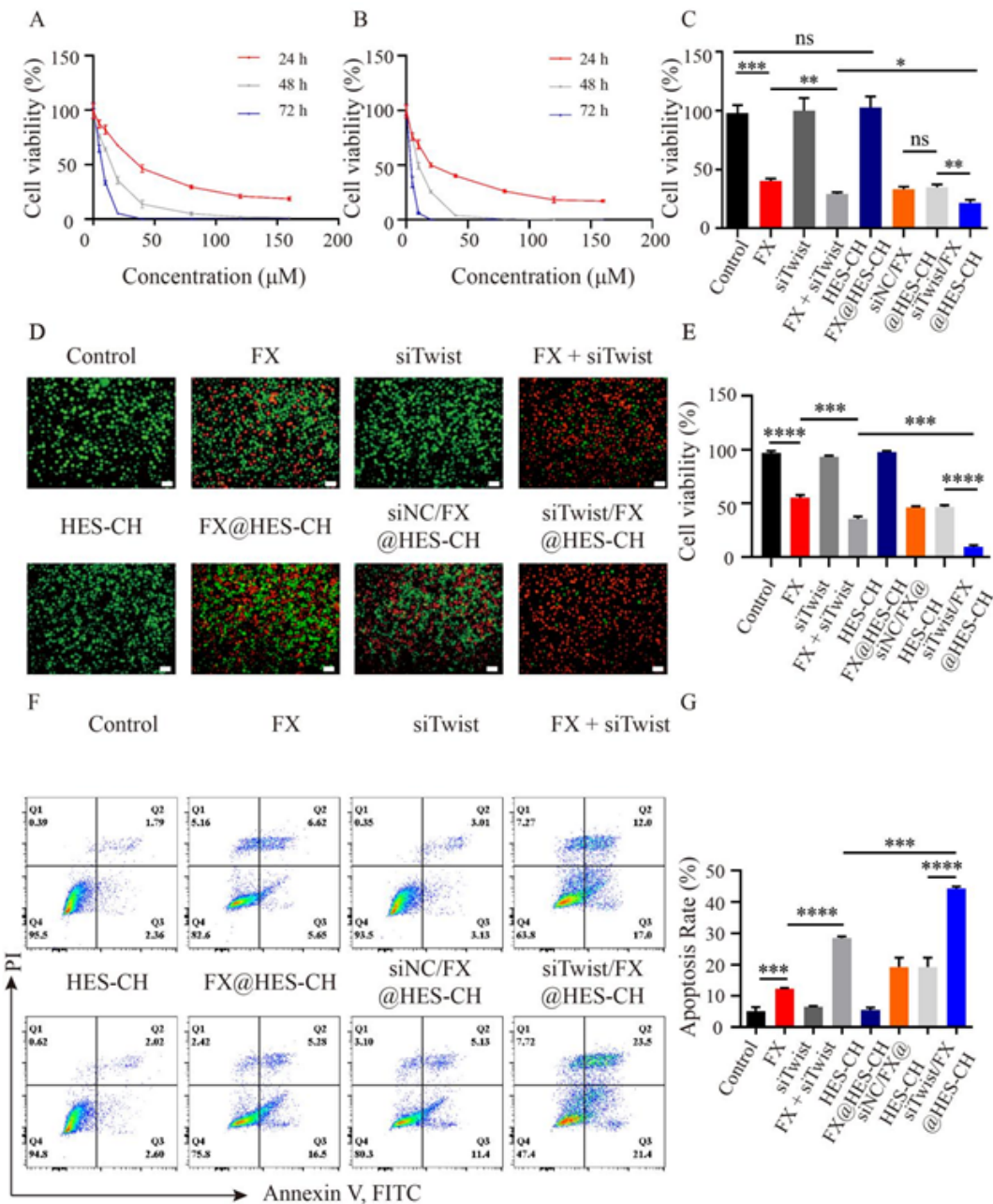


Figure 2

(A) The cytotoxicity of free FX against 4T1 cells after 24, 48, 72 h of incubation at various doses. (B) Cytotoxicity of siTwi/FX@HES-CH against 4T1 cells after 24, 48, and 72 h of incubation at varied FX doses. (C) Viability of 4T1 cells after 48 h treated with PBS, free FX, siTwi, free FX + siTwi, HES-CH, FX@HES-CH, siNC/FX@HES-CH, and siTwi/FX@HES-CH. (D) Live/death cell analysis of 4T1 cells treated with PBS, free FX, siTwi, free FX + siTwi, HES-CH, FX@HES-CH, siNC/FX@HES-CH, and

siTwist/FX@HES-CH and (E) quantitative analysis. Scale bar, 50 μ m. (F) Annexin V-FITC/PI apoptosis analysis of 4T1 cells treated with PBS, free FX, siTwist, free FX + siTwist, HES-CH, FX@HES-CH, siNC/FX@HES-CH, and siTwist/FX@HES-CH after 24 h and (G) quantitative analysis. All data were expressed as means \pm SD (n = 3). *p<0.05, **p<0.01, ***p < 0.001, and ****p < 0.0001 were considered to be statistically significant.

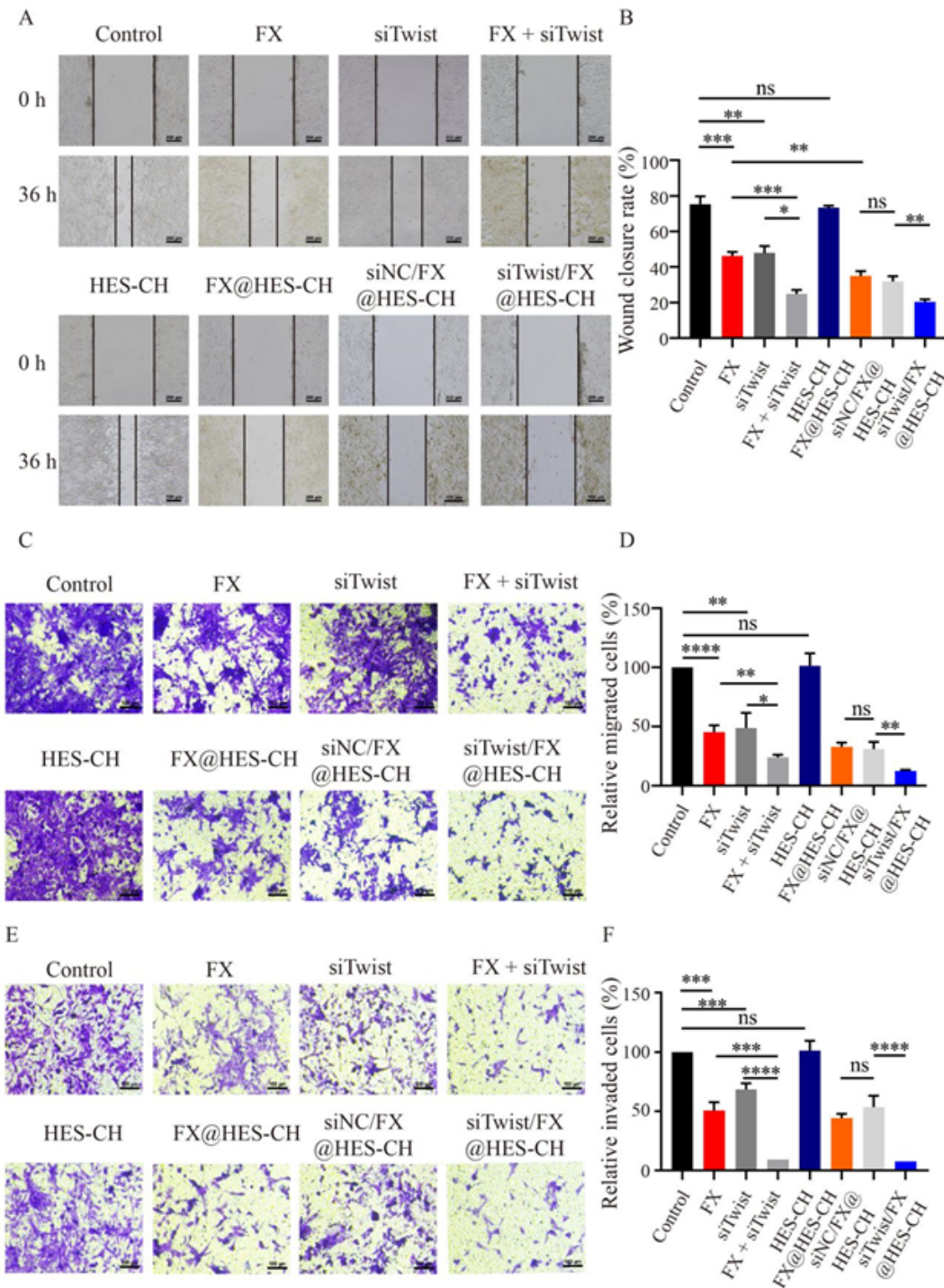


Figure 3

In vitro anti-metastasis effect of siTwist/FX@HES-CH on 4T1 cells. (A) Representative images of wound-healing assay and (B) quantitative analysis. Scale bar, 100 μm . (C) Representative images of Transwell migration assay and (D) quantitative analysis. Scale bar, 100 μm . (E) Representative images of Transwell invasion assay and (F) quantitative analysis. Scale bar, 100 μm . * $p < 0.05$, ** $p < 0.01$, *** $p < 0.001$ and **** $p < 0.0001$ were considered to be statistically significant.

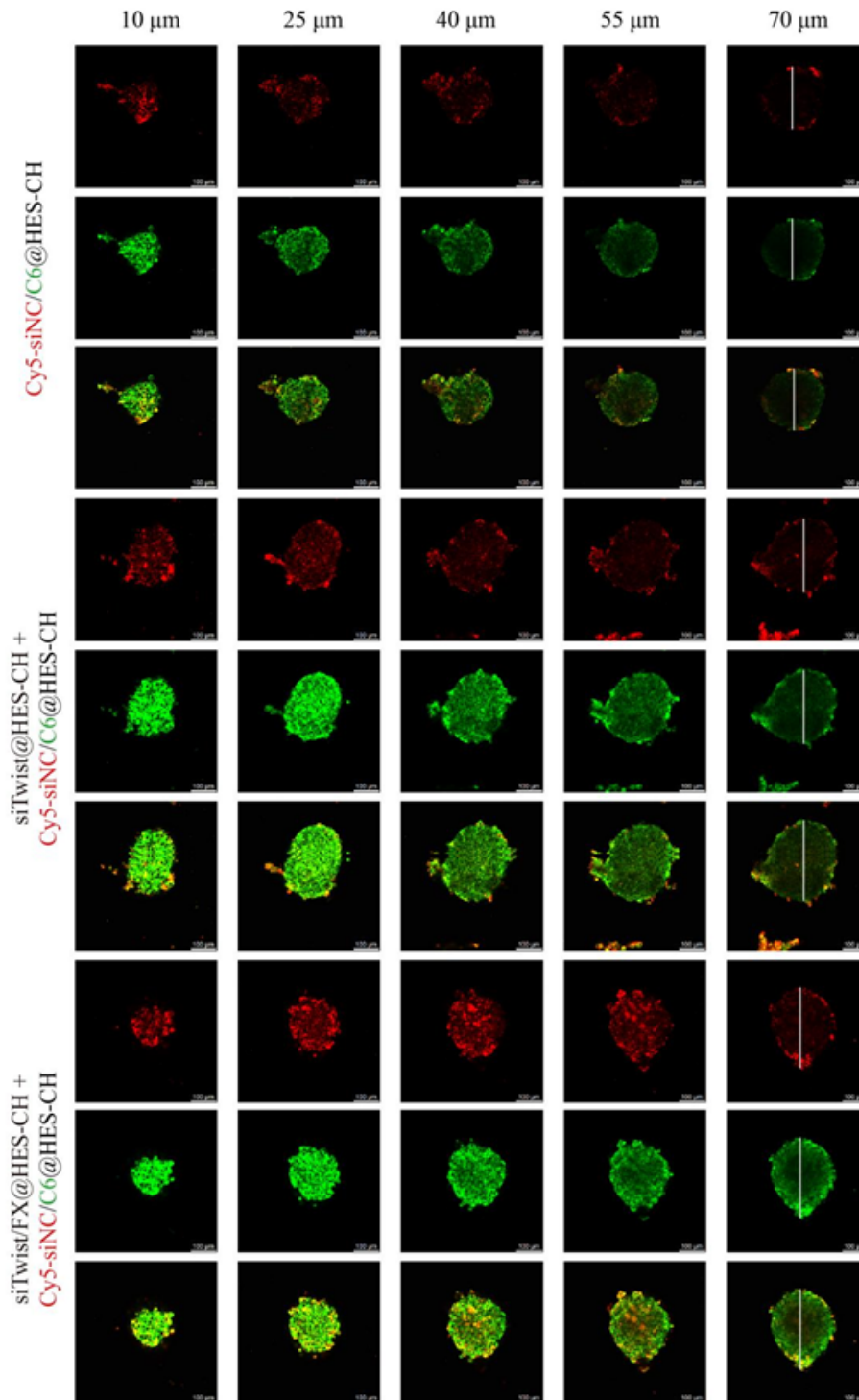


Figure 4

In vitro three-dimensional multicellular tumor spheroids penetration of Cy5-siNC/C6@HES-CH. Tumor spheroids were incubated with Cy5-siNC/C6@HES-CH for 48 h, concurrently administered with PBS, siTwist@HES-CH (containing 100 nM siTwist) and siTwist/FX@HES-CH (containing 100 nM siTwist and 20 μ M FX). The tumor spheroid model was established by mixing 4T1 cells with NIH/3T3 fibroblasts. Green fluorescence represents C6, and red fluorescence represents Cy5-siNC.

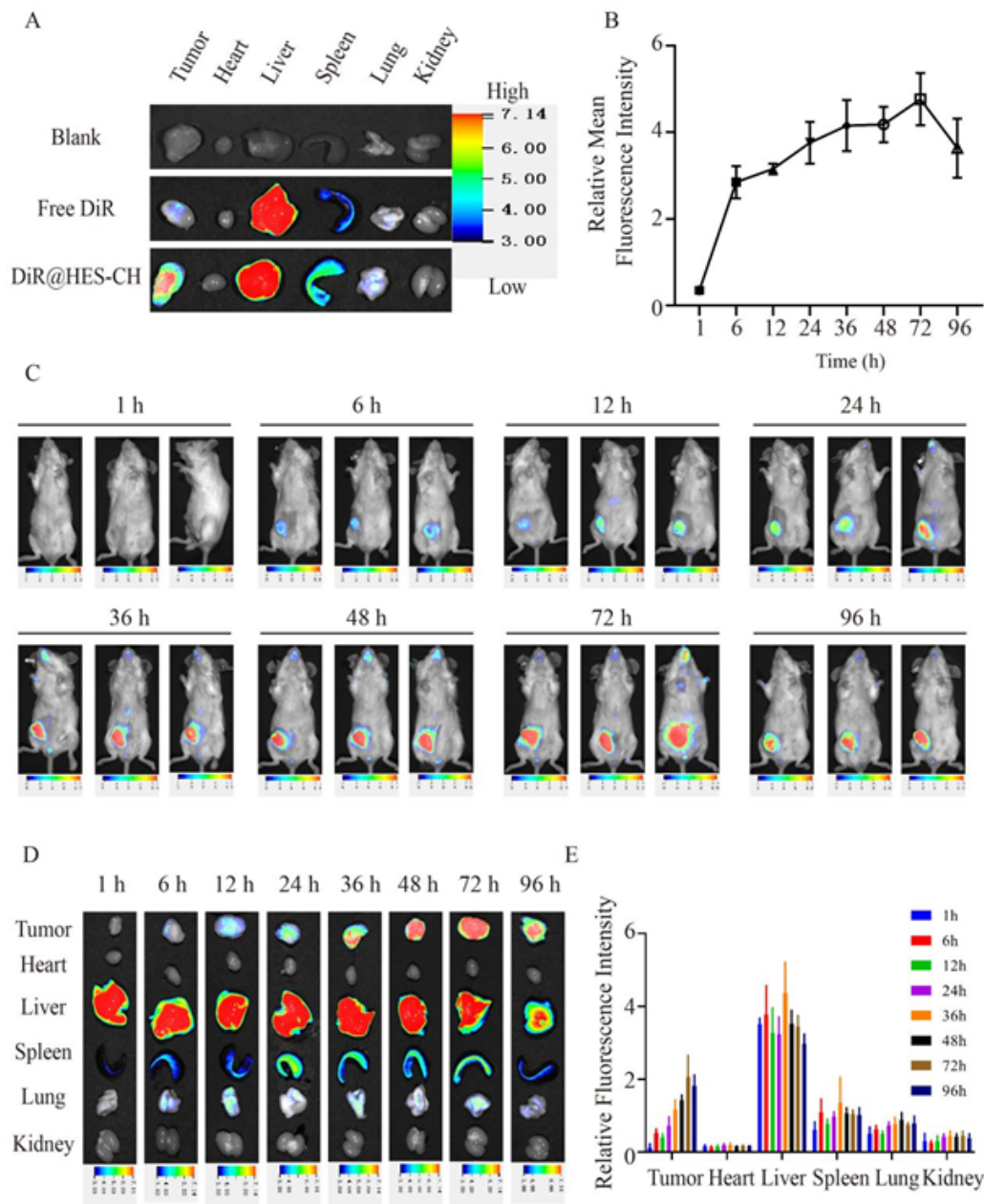


Figure 5

(A) *Ex vivo* fluorescence images of tumor and organs in 4T1 tumor-bearing mice at 48 h after intravenously administrated with PBS, free DiR, and DiR@HES-CH. (B) Representative bioluminescence images of tumor-bearing mice at 1, 6, 12, 24, 36, 48, 72, and 96 h after DiR@HES-CH injection. (C) Quantitative analysis of the bioluminescence signal in tumor-bearing mice. (D) Representative *ex vivo* bioluminescence images of isolated organs at 1, 6, 12, 24, 36, 48, 72, and 96 h after DiR@HES-CH injection. (E) Quantitative analysis of the bioluminescence signal in isolated organs. All data are shown as mean \pm SD (n = 3).

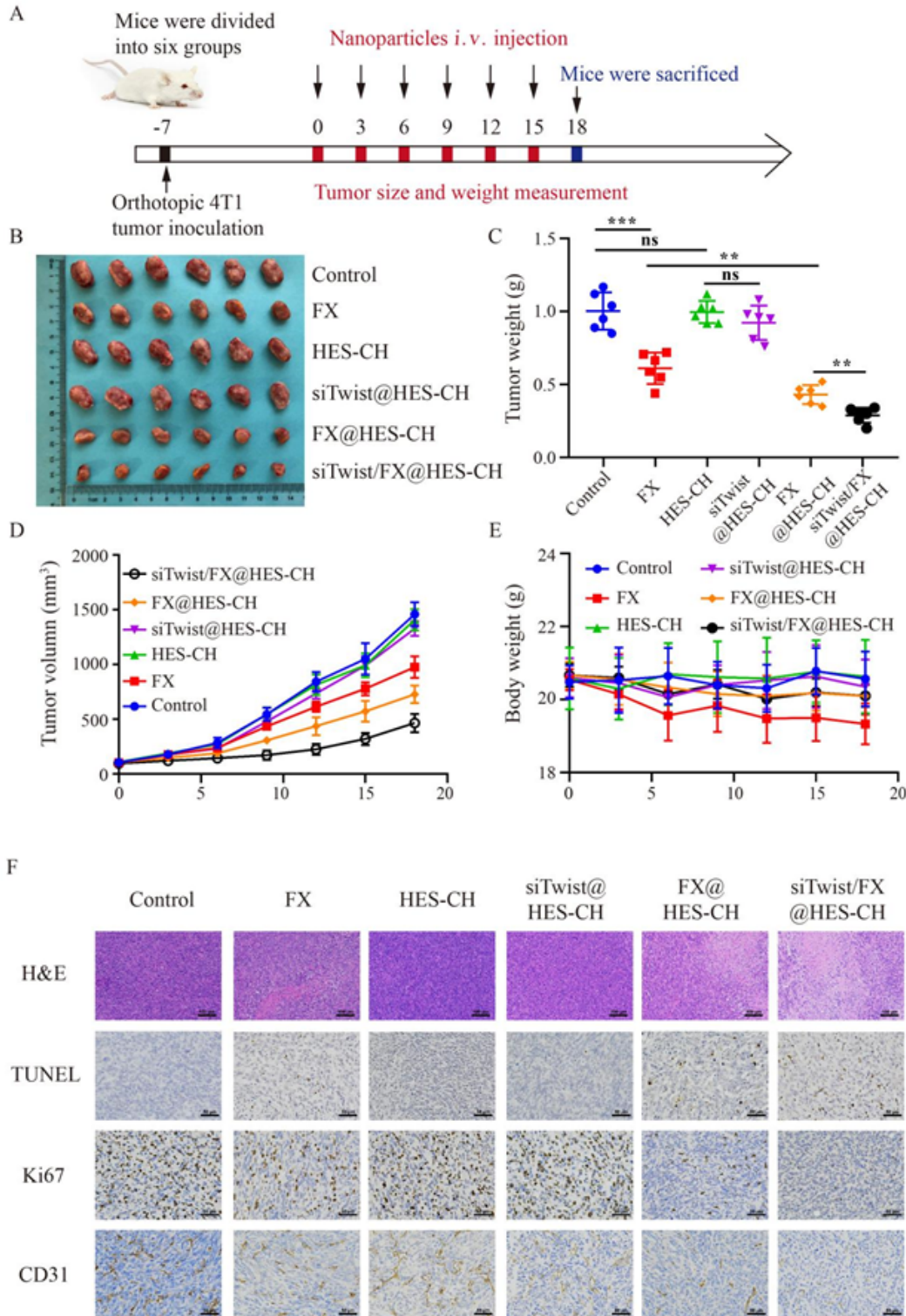


Figure 6

The anti-tumor effect in mice bearing 4T1 mammary tumors. (A) Schematic design of orthotopic tumor therapy model. (B) Representative image of excised orthotopic TNBC tumors from mice treated with saline (Control), free FX, HES-CH, siTwist@HES-CH, FX@HES-CH, or siTwist/FX@HES-CH under an 18-day treatment regimen (n = 6 per group) at the end of the therapy period, respectively. (C) Tumor weights in each group at the end of the treatment period. (D) Tumor progression was monitored by tumor volume measurement using caliper. (E) Body weight during the therapy period. (F) Tumor apoptosis, proliferation and angiogenesis evaluated by H&E (scale bar, 100 μ m), TUNEL, Ki67 and CD31 immunohistochemistry staining (scale bar, 50 μ m) of primary tumors in 4T1 mice mammary fat pad. All data are shown as mean \pm SD. *p < 0.05, **p < 0.01, ***p < 0.001 were considered to be statistically significant.

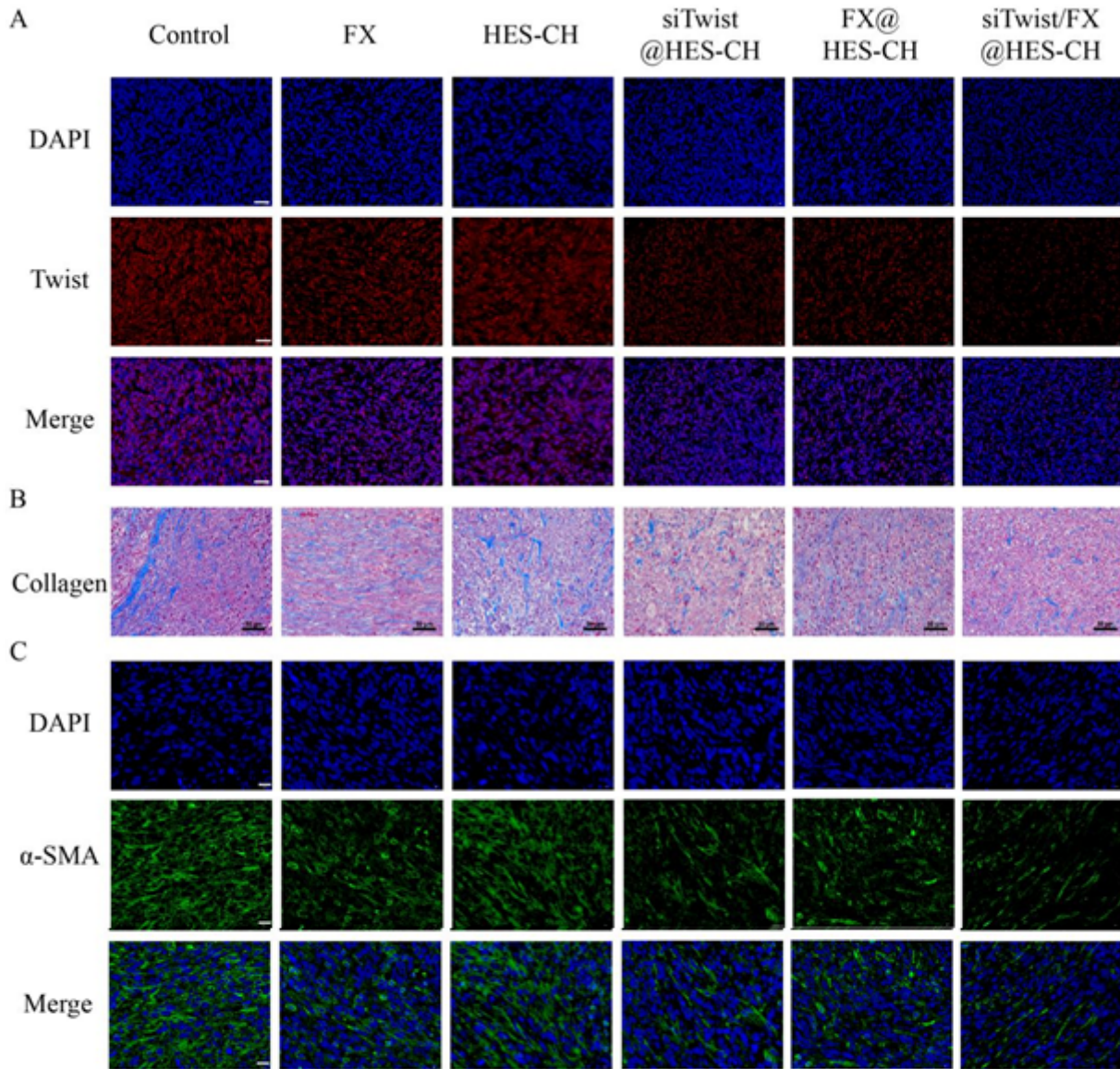


Figure 7

Representative images of Twist (A), collagen (B) and α -SMA (C) staining of 4T1 tumor after treatment with different formulations. Twist-positive cells were stained red fluorescence. Scale bars, 40 μ m. Collagen was stained using Masson's trichrome. The blue lines represent collagen. Scale bar, 50 μ m. α -SMA-positive cells were stained green fluorescence. Scale bar, 20 μ m.

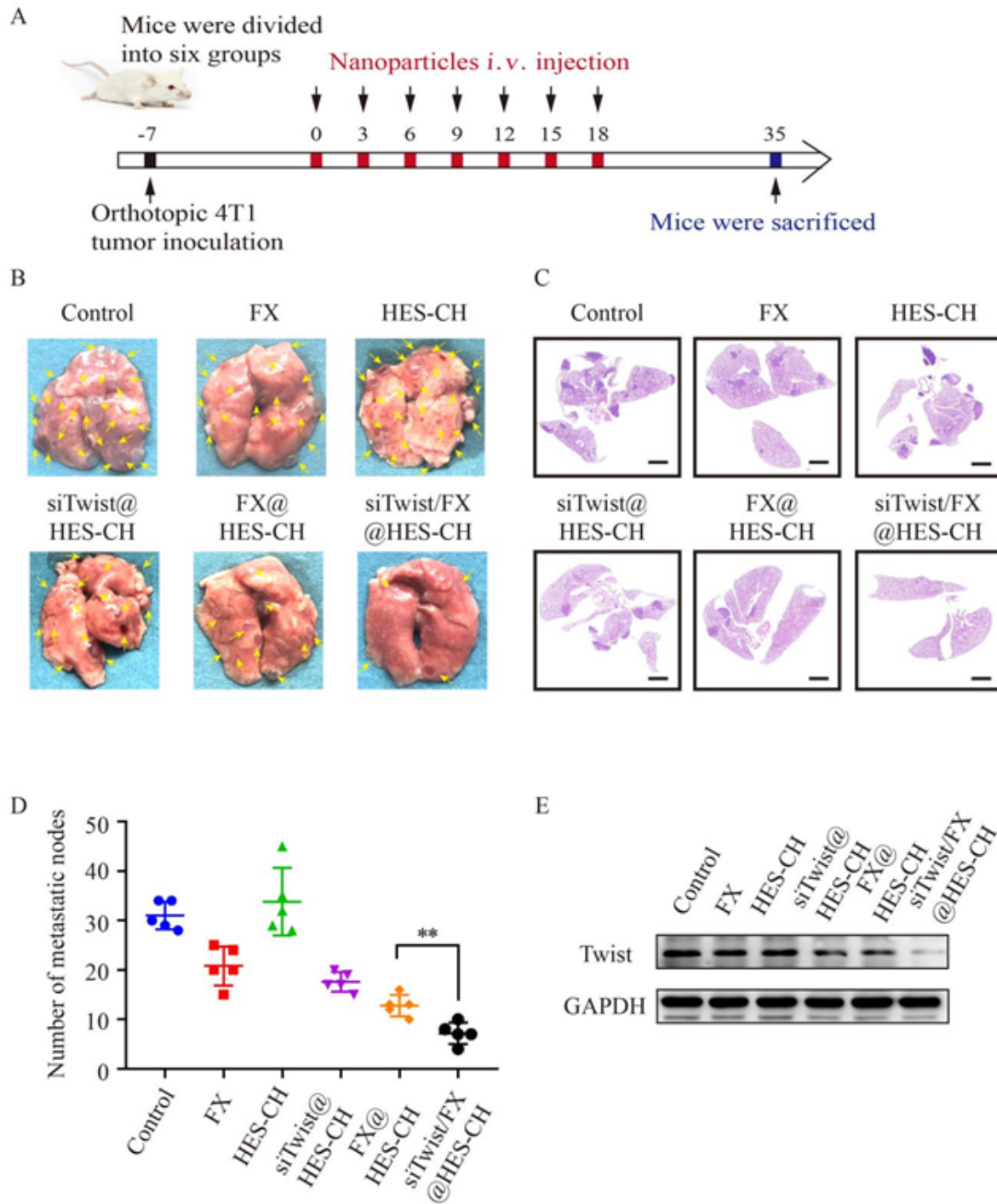


Figure 8

siTwist/FX@HES-CH inhibit lung metastasis of TNBC. (A) Schematic design of TNBC lung metastasis therapy. (B) Photographs of metastatic nodules in lungs. The yellow arrow denotes the metastatic nodules. (C) Histological assessment of lung metastatic nodules *via* H&E staining. Scale bar, 2000 μ m. (D) Numbers of the lung metastatic nodules. (E) Protein expression of Twist in primary tumors after different treatments.

Supplementary Files

This is a list of supplementary files associated with this preprint. Click to download.

- [Additionalfile1.docx](#)
- [Scheme1.png](#)
- [GraphicalAbstract.tif](#)
- [SchemeS1.tif](#)
- [FigureS1.tif](#)
- [FigureS2.tif](#)
- [FigureS3.tif](#)
- [FigureS4.tif](#)
- [FigureS5.tif](#)
- [FigureS6.tif](#)
- [FigureS7.tif](#)
- [FigureS8.tif](#)
- [FigureS9.tif](#)
- [FigureS10.tif](#)
- [FigureS11.tif](#)